CHAPTER W17

# Magnetic Materials

## W17.1 Details on Domain Structures

If $N_d$ is the number of domains in the array shown in Fig. 17.2*b* in the textbook,[†] there will be $(N_d - 1)$ domain walls, each of area $lt$, in the ferromagnetic film. When $N_d \gg 1$, the total energy associated with the domain walls will be

$$U_w = N_d \sigma_w lt = \frac{\sigma_w V}{d}, \tag{W17.1}$$

where $d$ is the width of each domain, $V$ is the total volume, and $N_d = w/d$. The total magnetic energy of the ferromagnetic film will then be

$$U = U_m + U_w = \frac{0.136 \mu_0 M_s^2 V d}{t} + \frac{\sigma_w V}{d}. \tag{W17.2}$$

When the energy $U$ is minimized with respect to $d$, the following results are obtained:

$$d = \frac{2.71}{M_s} \sqrt{\frac{\sigma_w t}{\mu_0}}, \tag{W17.3}$$

$$U = 0.738 V M_s \sqrt{\frac{\mu_0 \sigma_w}{t}}. \tag{W17.4}$$

If the energy $U$ is less than the energy $U_m$ for the single domain given in Eq. (17.4), the domain structure shown in Fig. 17.2*b* will be favored over the single domain shown in Fig. 17.2*a*. This will be true and expressions (W17.3) and (W17.4) will be valid as long as the domain wall surface energy $\sigma_w$ is not too large, that is, as long as

$$\sigma_w < 0.46 \mu_0 M_s^2 t. \tag{W17.5}$$

The actual domain structure found in a ferromagnetic solid can be very complicated and cannot in general be predicted beforehand except in very simple cases.

[†] The material on this home page is supplemental to *The Physics and Chemistry of Materials* by Joel I. Gersten and Frederick W. Smith. Cross-references to material herein are prefixed by a "W"; cross-references to material in the textbook appear without the "W."

## W17.2 Details on Size and Shape Effects

A straightforward estimate for an upper limit to the coercive field $H_c$ for a small magnetic particle can be obtained by noting that the effects of anisotropy can be overcome by a magnetic field **H** applied in the direction opposite to the direction of **M** along an easy axis. It has been shown[†] that the magnetic field, which leads to a reversal of the magnetization via the rotation of $\mathbf{M}_s$, is equal to the effective shape anisotropy field $H_s$ when the direction of the applied field **H** is opposite to the direction of $\mathbf{H}_s$ and **M**. Thus $H_s$ can be taken as an upper limit to the coercive field $H_c$. The corresponding predictions for $H_c$ are summarized in Table W17.1 for the three different types of magnetic anisotropy discussed in Section 17.5. Values of $H_c$ calculated for small Fe particles from these predictions are also included.

It can be seen that the coercive fields due to the anisotropies associated with crystal structure and with applied stress are both inversely proportional to $M_s$ while $H_c$ resulting from particle shape anisotropy is directly proportional to $M_s$. For the case of a collection of noninteracting randomly oriented particles, $H_c$ is reduced below its value for a single particle. Coercive fields can also be reduced by the magnetic interactions between individual particles in a powder, the effect being greater the denser the packing. Note that for the case of particle-shape anisotropy, the coercive field is a maximum for a long circular cylinder ($N_\perp = \frac{1}{2}$, $N_\parallel = 0$) magnetized along its length. In this case, $H_c = M_s/2$.

The contributions of surfaces and interfaces to the magnetocrystalline and magnetoelastic anisotropies can be important in magnetic thin films and multilayers. For example, in Au/Co/Au sandwiches the easy axis in the Co film is out of the plane for Co thicknesses of about six atomic layers and less. This has been attributed to magnetocrystalline

**TABLE W17.1 Estimates Predicted for the Upper Limit of the Coercive Fields $H_c$ of Small Magnetic Particles**

| Type of Anisotropy | $H_c$[a] | Typical Value[b] (kA/m) |
|---|---|---|
| Magnetocrystalline | | |
| Single particle | $\dfrac{2K_1(\text{or } K_u)}{\mu_0 M_s}$ | 39 |
| Randomly oriented Particles ($K_1 > 0$) | $\dfrac{0.64K_1(\text{or } K_u)}{\mu_0 M_s}$ | 25 |
| Particle shape | | |
| Single particle | $(N_\perp - N_\parallel)M_s$ | 855 |
| Randomly oriented particles | $0.48(N_\perp - N_\parallel)M_s$ | 410 |
| Applied stress | $\dfrac{3\lambda\sigma}{\mu_0 M_s}$ | 3.6 |

[a] $K_1$ and $K_u$ are the magnetocrystalline anisotropy coefficients for cubic and uniaxial ferromagnets, respectively.

[b] The parameters used are those appropriate for Fe at $T = 300$ K: $K_1 = 4.2 \times 10^4$ J/m$^3$, $M_s = 1710$ kA/m, magnetostriction $\lambda \approx 2 \times 10^{-5}$, yield strength $\sigma_y = 1.3 \times 10^8$ N/m$^2$. For the case of shape anisotropy, the particle shape corresponds to a long needle with $N_\perp = \frac{1}{2}$ and $N_\parallel = 0$.

[†] C. Kittel, *Rev. Mod. Phys.*, **21**, 541 (1949).

anisotropy related to the orbital component of the magnetic moment. This type of magnetocrystalline anisotropy results from the anisotropic bonding in multilayers such as Au/Co/Au and the spin–orbit interaction. In thicker Co films the shape-induced in-plane anisotropy dominates the orbital anisotropy and the easy axis is in-plane.

When the easy axes are the same for the magnetocrystalline and shape anisotropy effects, as might be the case in a long, needle-shaped particle, the coercive field is predicted to be enhanced since these anisotropy effects are then additive. In this case, $H_c$ would be given by

$$H_c = \frac{2K_1(\text{or } K_u)}{\mu_0 M_s} + (N_\perp - N_\parallel)M_s. \tag{W17.6}$$

Measured values of $H_c$ are often found to fall well below those predicted in Table W17.1, which correspond to the coherent rotation of **M**. These lower values of $H_c$ are usually due to domain nucleation associated with defects. In other mechanisms for the reversal of the magnetization that can occur at lower fields, the rotation of **M** is noncoherent (i.e., it occurs in a spatially nonuniform manner within the material).[†]

## W17.3 Details on Magnetostriction

The magnetostriction of single-crystal $Fe_{1-x}Ni_x$ alloys with $x = 0.6$ and 0.85 is, in fact, observed to be isotropic. For the $Fe_{0.4}Ni_{0.6}$ alloy $\lambda$ is large and positive, while for the $Fe_{0.15}Ni_{0.85}$ alloy magnetostriction is essentially absent (i.e., $\lambda \approx 0$). For completely random polycrystalline materials which can be expected to be both elastically and magnetically isotropic, the *isotropic magnetostriction* is given by

$$\lambda = \frac{2\lambda_{100}}{5} + \frac{3\lambda_{111}}{5}, \tag{W17.7}$$

where $\lambda_{100}$ and $\lambda_{111}$ correspond to single crystals of the same material.

While an applied stress can affect the state of magnetization in a magnetic material, it does not affect the value of the spontaneous magnetization $M_s$ in the elastic limit. Changes in $M_s$ can occur in the inelastic regime, however, but only when the applied stress is large enough to cause a structural phase transition. When $K_\sigma > K_1$ or $K_{u1}$ for the magnetocrystalline anisotropy, the effect of the applied stress can be large enough to change the direction of the easy axis away from that corresponding to the magnetocrystalline anisotropy.

The dependence of the linear magnetostriction $\delta l/l$ on applied magnetic field for the rare earth ferromagnet $Tb_{0.6}Dy_{0.4}$ is shown at $T = 77$ K in Fig. W17.1 for two different stresses applied to an *a*-axis rod. The magnetization and magnetostriction both reach saturation at essentially the same magnetic field. The observed changes in $\delta l/l$ result from the changing state of the magnetization in the material as the applied field is increased and the magnetic domains are aligned in the direction of **H**. When the magnetization is saturated, the observed magnetostriction also reaches its saturation value $\lambda$, as shown.

When a magnetic field **H** is applied perpendicular to the easy *c* axis of a crystalline uniaxial ferromagnet such as Co, the development of the macroscopic magnetization

[†] I. S. Jacobs and C. P. Bean, *Phys. Rev.*, **100**, 1060 (1955).

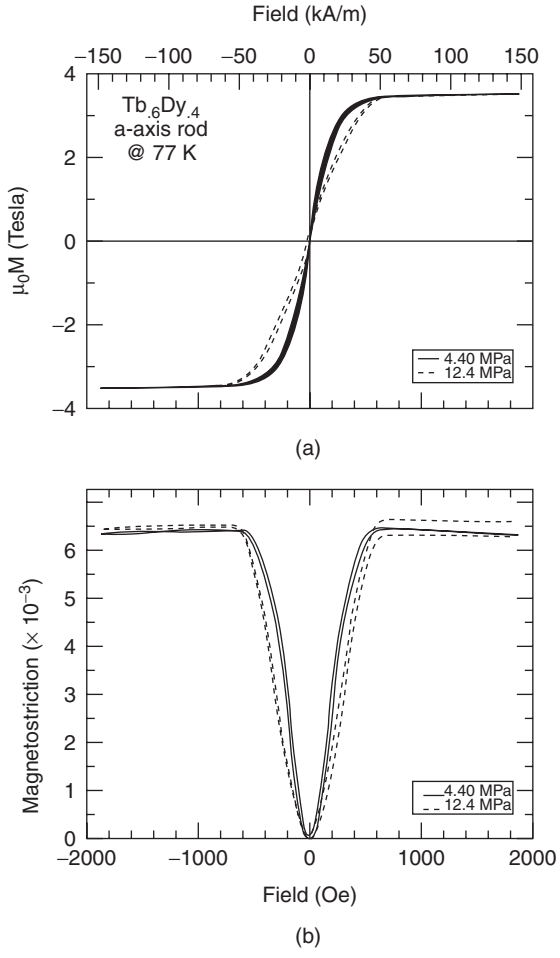


**Figure W17.1.** Dependencies of the magnetization $M$, (*a*), and magnetostrictive strain $\delta l/l$, (*b*), on applied magnetic field at $T = 77$ K for the rare earth ferromagnet $Tb_{0.6}Dy_{0.4}$ are presented for two different stresses (MPa = megapascals) applied to an *a*-axis rod. (Note that the magnetization is actually plotted as $\mu_0 M$ and that the field scales are the same in (a) and (b)). [From A. E. Clark et al., *IEEE Trans. Magn.* **MAG-22**, 3156 (1992). Copyright 1992 by IEEE.]

**M** takes place solely by rotation of the individual domain magnetizations. In this case the dependence of the fractional change in length is given in terms of $M$ by

$$\frac{\delta l}{l} = \frac{3\lambda}{2}\left(\frac{M}{M_s}\right)^2. \tag{W17.8}$$

For cubic ferromagnets with magnetocrystalline anisotropy coefficients $K_1 > 0$, the dependence of $\delta l/l$ on $M/M_s$ is determined by the relative ease with which 90° and 180° domains walls move. A useful discussion of the phenomenology of magnetostriction is given in Chikazumi (1964 Chap. 8). The topic of volume magnetostriction is also covered by Chikazumi.

## W17.4 Giant and Colossal Magnetoresistance

So-called *giant negative magnetoresistance* (GMR) effects in magnetically inhomogeneous materials, first observed in metallic Fe/Cr magnetic multilayers, typically correspond to changes in the ratio $[R(0) - R(H)]/R(H)$ by 100 to 1000% in fields of about $1.6 \times 10^3$ kA/m. These effects arise from changes in the spin-dependent scattering of the conduction electrons as a result of an applied magnetic field that affects the orientation of the magnetization **M** in the ferromagnetic Fe layers. Experimental results for the GMR effect in three different Fe/Cr multilayers at $T = 4.2$ K are shown in Fig. W17.2. The longitudinal magnetoresistance and the magnetization of these multilayers reach saturation at the same magnetic field $H_s$. It can be seen that the magnitude of the magnetoresistance changes with the thickness of the nonferromagnetic Cr layer. In fact, the magnitude of the GMR effect oscillates as the thickness of the Cr layer is increased. This is attributed to an interlayer exchange coupling that oscillates between ferromagnetic and antiferromagnetic. Only multilayers for which the interlayer coupling is antiferromagnetic display large GMR effects, apparently due to the fact that only in these systems can the coupling be changed significantly by an applied magnetic field.

The scattering processes that give rise to the GMR effect are believed to take place at the interfaces between the ferromagnetic layers and the adjacent nonferromagnetic or nonmagnetic layers rather than within the ferromagnetic layers themselves. In fact, the magnetoresistance of the Fe/Cr multilayers is much greater than the intrinsic magnetoresistance of the Fe layers themselves. The resistance of the multilayer structure is higher when the magnetizations in the ferromagnetic layers are antiparallel and lowest when they are parallel. A wide variety of transition metal magnetic-multilayer systems have been observed to demonstrate the GMR effect, including Co/Cu, which exhibits very large GMR effects even at room temperature. In fact, Co/Cu multilayers are now used in magnetic read heads for the detection of magnetic bits on hard disks, as described in Sections 17.12 and W17.12.

The phenomenon of *colossal magnetoresistance* (CMR), with observed magnetic field-induced decreases of resistance in the range $10^5$ to $10^6$%, have been observed

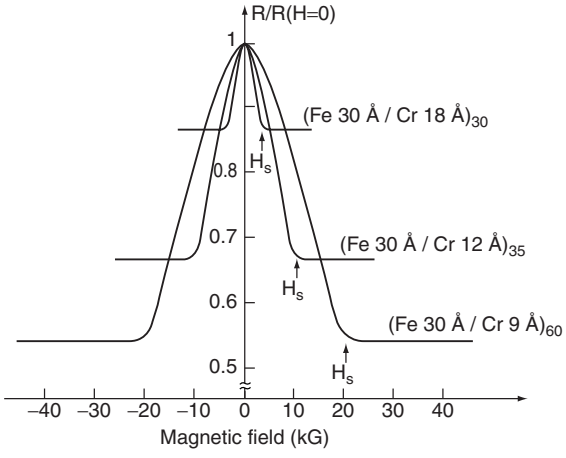


**Figure W17.2.** Experimental observations of giant longitudinal magnetoresistance $R(H)/R(0)$ in three different (001)Fe/(001)Cr magnetic multilayers at $T = 4.2$ K. [From M. N. Baibich et al., *Phys. Rev. Lett.*, **61**, 2472 (1988). Copyright 1988 by the American Physical Society.]

in ceramic magnetic materials of the form $A_{1-x}B_xMnO_3$ (e.g, $La_{1-x}Ca_xMnO_3$), which have the cubic perovskite crystal structure shown in Fig. 15.6. Here A and B are trivalent rare earth and divalent alkaline earth ions, respectively. In these CMR materials, magnetic ions such as Mn can exist in more than one valence state (e.g., as $Mn^{3+}$ and $Mn^{4+}$ in $La_{1-x}Ca_xMnO_3$). The change in valence from $Mn^{3+}$ to $Mn^{4+}$ occurs as the $La^{3+}$ ions are replaced by $Ca^{2+}$ ions. The effects of an applied field $H$ on the ordering and alignment of the spins of the magnetic ions determine the magnitude of the CMR effect. Conduction in these oxides is proposed to take place by the hopping of $d$ electrons from $Mn^{3+}$ ions to neighboring $Mn^{4+}$ ions via intervening $O^{2-}$ ions. For hopping to occur, the spins of the two Mn ions involved must initially be parallel, thus demonstrating that the resistivity of the material will depend on its magnetic order. This indirect interaction between next-NN $Mn^{3+}$ and $Mn^{4+}$ ions is termed *double exchange* and is essentially a ferromagnetic interaction. The properties of these materials are very sensitive to inhomogeneities related to deviations from oxygen stoichiometry. It should be noted that $LaMnO_3$ itself is an antiferromagnetic insulator, while $La_{1-x}Ca_xMnO_3$ becomes ferromagnetic for $0.3 < x < 0.5$. Note that the superexchange interaction between next-NN $Mn^{2+}$ ions in MnO, described in Section 9.7, via the intervening $O^{2-}$ ions is an antiferromagnetic interaction.

It is possible that this CMR may result from a magnetic field–induced ferromagnetic metal–paramagnetic insulator transition.[†] The CMR effect occurs over a restricted range of temperatures near the transition. Starting from high $T$, as the temperature is lowered, evidence is found for the formation of small ferromagnetic clusters which are approximately 1.2 nm in diameter in $La_{0.67}Ca_{0.33}MnO_3$. The clusters are conducting but are isolated from each other. As the temperature is lowered still further, the number of these clusters grows until they percolate through the material at the transition temperature and form an infinite cluster. Above $T_c$ the material conducts weakly via carrier hopping from cluster to cluster, while below $T_c$, electrons are delocalized over the entire percolation cluster and the material conducts as a metal. The magnetic and *metal–insulator* (M–I) transitions do not occur at well-defined temperatures, with the M–I transition occurring at a slightly lower temperature.

The mechanism of the CMR is still an open area of research. In the high-temperature insulating state the spin-up and spin-down states are degenerate and both bands are fully occupied by Mn $3d$ electrons. The Fermi level lies above both bands. In the low-temperature ferromagnetic state, there is a splitting of the spin-up and spin-down bands. Spin-resolved photoemission studies have verified that the Fermi level lies in the interior of the majority-spin band, so that those electrons can conduct, whereas the minority-spin band lies below the Fermi level, and those electrons remain nonconducting. The material is said to be a *half-metal*. The unequal occupancy of the two bands leaves an unbalanced magnetic moment and the material becomes a ferromagnet, as shown in Fig. W17.3.

The magnetic moment of each cluster is randomly oriented in zero field. Hopping of electrons and holes from one cluster to another is inhibited since the spins of the clusters may not be aligned. Carriers from one cluster would have to hop an appreciable distance to find a suitably aligned cluster. The application of an external magnetic field serves to align the magnetic moments of the clusters and hence to reduce the effective hopping distance. This can account for the dramatic sensitivity of the conductivity

[†] For a useful review, see C. N. R. Rao et al., *Chem. Mater.*, **8**, 2421 (1996).

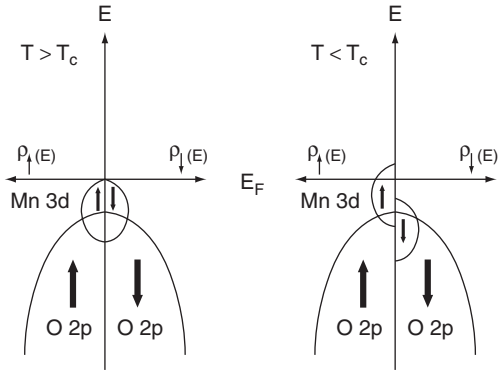


**Figure W17.3.** Schematic diagram of the Mn $3d$ and O $2p$ spin-up and spin-down energy bands in a $La_{1-x}Ca_xMnO_3$-type perovskite, both above and below the Curie temperature $T_C$. [Adapted from J. H. Park et al., *Nature*, **392**, 794 (1998).]

to external magnetic field and thus for the CMR phenomenon. The effect is most pronounced near $T_c$.

## W17.5 Faraday and Kerr Effects

***Faraday Effects.*** *Faraday rotation* usually corresponds to the rotation by an angle $\theta_F$ of the plane of polarization of a linearly polarized EM wave due to its transmission through a magnetic material (or through a suitable medium in the presence of a magnetic field). Faraday rotation in nonmagnetic materials is described in Chapter W18. For the polar Faraday effect the Faraday rotation $\theta_F$ is usually defined to be one half of the change in phase angle $\phi$ between the right and left circularly polarized waves due to transmission. This is given by

$$\theta_F = \frac{\phi_+ - \phi_-}{2} = \frac{\pi(n_+ - n_-)d}{\lambda}, \tag{W17.9}$$

where $\lambda$ is the wavelength in vacuum, $d$ the sample thickness, and $n_+$ and $n_-$ the real parts of the complex indices of refraction for right and left circularly polarized light, respectively. The difference $(n_+ - n_-)$ is called the *magnetic circular birefringence* (MCB).

When the absorption of light in the material is small, the Faraday rotation is

$$\theta_F = \frac{-\sigma'_{xy}d}{2nc\epsilon_0}. \tag{W17.10}$$

Here $\sigma'_{xy}$ is the real part of $\sigma_{xy}$, an off-diagonal component of the complex conductivity tensor $\sigma$, $n$ is the average of $n_+$ and $n_-$, and $\epsilon_0$ is the permittivity of free space.[†] The quantity $\sigma_{xy}$ is in general linear in the magnetization $M$ of the material. When the

[†] In SI units the complex conductivity tensor $\sigma(\omega)$ is related to the complex dielectric function tensor $\epsilon_r(\omega)$ by $\sigma(\omega) = -i\omega\epsilon_0[\epsilon_r(\omega) - 1]$.

induced magnetization $M$ is linear in the applied field $H$, as in paramagnetic and diamagnetic materials, both $\sigma_{xy}$ and $\theta_F$ are also linear in $H$. The Faraday rotation is then expressed as

$$\theta_F = VHd, \tag{W17.11}$$

where $V$ is the *Verdet constant*, usually expressed in the non-SI units of arcminutes/oersted·m [see Eq. (W18.12) and Table W18.1]. Note that $V$ can depend on temperature through the magnetic susceptibility of the material and on the wavelength $\lambda$ of the light through the optical constants of the material. In general, $\theta_F$ will be given by $VMd$, where $M$ is the magnetization of the material.

*Magnetic circular dichroism* (MCD) corresponds to the difference in the absorption of light with right and left circular polarizations, also in the polar geometry. When the absorption is small, the difference in the absorption coefficients is given by

$$\alpha_+ - \alpha_- = \frac{\sigma''_{xy}}{c\epsilon_0}, \tag{W17.12}$$

where $\sigma''_{xy}$ is the imaginary part of $\sigma_{xy}$. The MCD or Faraday ellipticity effect will also transform linearly polarized light into elliptically polarized light. When employed with circularly polarized x-rays, MCD is known as *XMCD spectroscopy* and is a technique that can be used to determine element-specific spin and orbital magnetic moments and their anisotropies in a quantitative manner. Since XMCD can have submonolayer sensitivity, it is a useful technique for studying magnetism at surfaces and in thin films, including the direction of easy magnetization in thin films and magnetic imaging.

For the longitudinal or transverse Faraday geometries, the observed effects are quadratic in $M$ or $H$ and are referred to as *magnetic linear birefringence* (MLB) and *magnetic linear dichroism* (MLD). These effects are not discussed here. For a summary of the MLB and MLD effects, see Craig (1991).

***Kerr Effects.*** *Magneto-optical Kerr effects* (MOKEs) correspond to changes in the state of polarization of electromagnetic waves associated with their reflection from the surfaces of magnetic materials. The Kerr signal is proportional to the average surface magnetization of the material and to its reflectivity. Typical geometries for the polar, transverse, and longitudinal Kerr effects are illustrated schematically in Fig. 17.16.

In the *polar Kerr effect* geometry the magnetization **M** of the ferromagnet is oriented perpendicular to its surface. In this case, when the incident EM wave is linearly polarized, the reflected wave will be elliptically polarized and the major axis of the resulting ellipse will be rotated either clockwise or counterclockwise, depending on the direction of **M**. The *polar Kerr rotation* $\theta_K$ and *ellipticity* $\eta_K$ are given by

$$\theta_K + i\eta_K = \frac{i\epsilon_{xy}}{\sqrt{\epsilon_{xx}}(\epsilon_{xx} - 1)}, \tag{W17.13}$$

where the complex quantities $\epsilon_{xx}$ and $\epsilon_{xy}$ are diagonal and off-diagonal components of the complex dielectric function $\epsilon = \epsilon_1 + i\epsilon_2$. The angle of rotation of the major axis of the ellipse is

$$\theta_K = \frac{\lambda\sigma''_{xy}}{2\pi nc\epsilon_0}. \tag{W17.14}$$

This is similar in form to $\theta_F$ for the Faraday effect given in Eq. (W17.10), but with two important differences: the thickness $d$ in $\theta_F$ is replaced here by the wavelength $\lambda$ of the incident light, and the real part $\sigma'_{xy}$ of $\sigma_{xy}$ appearing in $\theta_F$ is replaced here by the imaginary or absorptive part $\sigma''_{xy}$. Note that for a transparent material, $\sigma''_{xy}$, and hence $\theta_K$, are both zero. The polar Kerr effect has the largest response of the three Kerr effects and, in addition, probes the component of the magnetization perpendicular to the surface of the material. Only the polar Kerr effect is nonzero for normal incidence.

In the *transverse Kerr effect* geometry, **M** is parallel to the surface of the magnetic material and is perpendicular to the incident plane of polarization of the EM wave. In the *longitudinal Kerr effect* geometry, **M** is also parallel to the surface but lies in the incident plane of polarization. The *Voigt effect* has the same geometry as the transverse Kerr effect but corresponds to the case of reflection from a nonabsorbing medium.

If the **E** field of the incident EM wave is perpendicular to the plane of incidence in the transverse Kerr geometry, the reflectivity $R$ will not be affected significantly by the magnetization of the material. If, however, the **E** field lies in the plane of incidence, $R$ will depend linearly on **M**. It follows therefore that when unpolarized light is incident on an absorbing magnetic material, the reflectivity $R$ measured for different regions will depend on the local direction of **M** (i.e., on the magnetic domain structure). This effect can be employed for the observation of magnetic domains in magnetic recording media. The Voigt effect is observed when the magnetic material is nonabsorbing. In this case the amount of linearly polarized light that is converted upon reflection to elliptically polarized light will be proportional to $M^2$. This corresponds to a type of *magnetic birefringence*.

The *surface* MO Kerr effect (SMOKE) is often used in conjunction with ultrahigh-vacuum techniques to probe the magnetic properties of surfaces. Phenomena that have been studied include the existence of surface magnetism, the magnetic anisotropy induced by and associated with surfaces, and the Curie temperature $T_C$ as a function of film thickness. Figure W17.4 shows magnetization curves of Fe/Mo/Fe multilayer films obtained via SMOKE. A square hysteresis loop is obtained when the two Fe layers are ferromagnetically aligned via coupling through the Mo layer. When

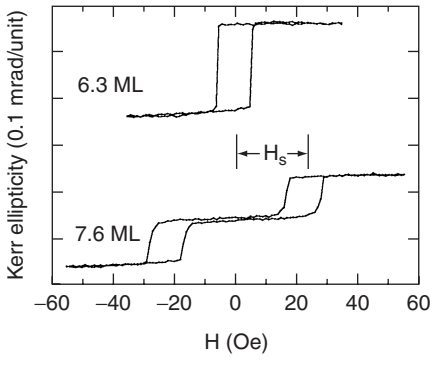


**Figure W17.4.** Magnetization curves of Fe/Mo/Fe multilayer films obtained via SMOKE. A square hysteresis loop is obtained when the two Fe layers are ferromagnetically aligned via coupling through the Mo layer. When the Mo layer is thicker, 7.6 monolayers (ML), the Fe layers couple antiferromagnetically and the switching field $H_s$ is required to return their alignment to ferromagnetic. (From Z. Q. Qiu and S. D. Bader, *Mater. Res. Soc. Bull.*, **20**(10), 34 (1995).)

the Mo layer is thicker (e.g., 7.6 monolayers) the Fe layers couple antiferromagnetically and the switching field $H_s$ is required to return their alignment to ferromagnetic.

## W17.6 Details on Dynamic Magnetic Effects

***Eddy Currents.*** The eddy currents generated in, for example, a long cylinder of a magnetic material by a changing magnetic field $H(t)$ can be calculated from electromagnetic theory using Faraday's law of induction. When the cylinder consists of a single magnetic domain and when the field $H$ penetrates the cylinder completely, the power loss per unit volume of the material due to the eddy currents can be expressed in terms of the changing magnetization $M$ by

$$p = \frac{P}{V} = \frac{\mu_0^2 r^2}{8\rho}\left(\frac{dM}{dt}\right)^2. \tag{W17.15}$$

Here $r$ is the radius of the cylinder and $\rho$ is the electrical resistivity of the material. When $M(t) = M_0 e^{-i\omega t}$, the power loss $p$ will be proportional to $\omega^2 M_0^2$. From this expression it is clear that eddy current losses in magnetic materials can be reduced by increasing the resistivity $\rho$ of the material.

When the cylinder has a magnetic microstructure consisting of more than one magnetic domain, the eddy current losses will be increased over the single-domain case due to localization of the currents induced in the vicinity of the domain walls. As domain walls move or as the magnetization within a domain rotates, the local time-dependent changes in $M$ and $H$ induce localized eddy currents whose distributions are very difficult to calculate. Localized eddy current losses will occur even if the magnetization loop is traversed slowly.

When the rates of change of $H$ and $M$ are very large, as at high frequencies, the magnetic fields resulting from the induced eddy currents will oppose the change in the applied field, thereby screening the applied field $H$ from the center of the solid. This is known as the *skin effect* and is most pronounced in conducting materials. The applied field $H$ and the corresponding changes in the magnetization $M$ will decrease to $1/e$ of their values at the surface within a distance $\delta$ known as the *skin depth*, given by

$$\delta = \sqrt{\frac{2\rho}{\omega\mu}}. \tag{W17.16}$$

Here $\mu$ is the magnetic permeability of the material. Since Fe is a magnetic material widely used in the cores of transformers, it is useful to note that $\delta \approx 0.9$ mm at $f = 60$ Hz, using $\rho(\text{Fe}) = 1 \times 10^{-7}$ $\Omega$·m and $\mu(\text{Fe})/\mu_0 \approx 500$ at $T = 300$ K. To allow for complete penetration of the magnetic field, transformer cores are therefore formed from thin, laminated sheets of Fe. In applications of magnetic materials at microwave frequencies, it is usually advantageous to employ materials with high resistivities such as magnetic ferrites in order to reduce the eddy current losses.

***Ferromagnetic Resonance.*** The magnetization vector $\mathbf{M}$ of a magnetic solid will undergo precession around the direction of the total static magnetic field $\mathbf{H}_{\text{tot}}$, as illustrated schematically in Fig. W17.5. The sources of $\mathbf{H}_{\text{tot}}$ can correspond to a combination of an applied field $\mathbf{H}$ and internal fields such as a demagnetizing field $\mathbf{H}_D$, an effective

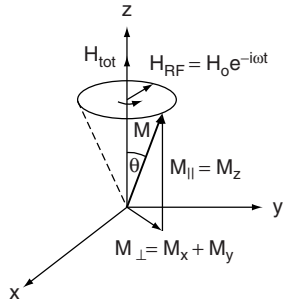


**Figure W17.5.** Precession of the magnetization vector **M** of a magnetic solid around the direction of a magnetic field $\mathbf{H}_{\text{tot}}$. An external RF magnetic field $H_{\text{RF}}(t)$ acting at right angles to the static field $\mathbf{H}_{\text{tot}}$ is also shown.

anisotropy field $\mathbf{H}_a$, and an effective molecular field $\mathbf{H}_{\text{eff}} = \mathbf{B}_{\text{eff}}/\mu_0$. This precessional motion is a consequence of the torque per unit volume $\boldsymbol{\tau}/V = \mu_0 \mathbf{M} \times \mathbf{H}_{\text{tot}}$ exerted on **M** by $\mathbf{H}_{\text{tot}}$ as described by the equation of motion:

$$\frac{d\mathbf{M}}{dt} = -\gamma\mu_0 \mathbf{M} \times \mathbf{H}_{\text{tot}}. \tag{W17.17}$$

Here $\gamma = ge/2m$ is the gyromagnetic ratio and $g$ is the Landé $g$ factor, given for an atom in Eq. (9.6). This expression is valid in the absence of any damping of the motion of **M**. For a long cylinder the precession of **M** occurs at an angular frequency given by

$$\omega = \gamma\mu_0 H_{\text{tot}}. \tag{W17.18}$$

In the presence of damping forces acting on **M**, energy will be transferred from the spin system (i.e., the magnetization) to the lattice or to the electrons. Examples of possible loss mechanisms include eddy currents, excitation of spin waves, and so on. These energy losses can be compensated by the application of a transverse radio-frequency magnetic field $H_{\text{RF}}(t) = H_0 e^{-i\omega t}$ acting at right angles to the static field $\mathbf{H}_{\text{tot}}$ (see Fig. W17.5). As the frequency $\omega$ of $H_{\text{RF}}$ is varied, resonance will occur at $\omega = \omega_r = \gamma\mu_0 H_{\text{tot}}$, at which point the spin system absorbs the maximum amount of energy from the microwave field. For $g = 2$ and $\gamma = 1.76 \times 10^{11}$ C/kg, the resonant frequency is $\omega_r = 2.21 \times 10^{11}$ Hz in a typical field of $H_{\text{tot}} = 10^3$ kA/m. This frequency corresponds to a wavelength $\lambda = 8.54$ mm (i.e., to microwave radiation). The full-width at half maximum of the resonance peak in $\chi''$ is proportional to the magnitude of the damping while the magnitude of $\chi''$ at resonance is inversely proportional to the damping.

One important application of the resonant absorption of EM radiation by a ferromagnet (i.e., of a *ferromagnetic resonance* measurement) is the determination of the $g$ factor, $g = 2m\omega_r/e\mu_0 H_{\text{tot}}$. Results obtained for the $3d$ transition metal ferromagnets are $g(\text{Fe}) = 2.10$, $g(\text{Co}) = 2.18$, and $g(\text{Ni}) = 2.21$. These values indicate that the magnetization in these materials is associated primarily with the spin magnetic moment $m_{\text{spin}}$ of the electron. In fact, measurements of the $g$ factor by ferromagnetic resonance allow the ratio $\varepsilon = m_{\text{orb}}/m_{\text{spin}}$ of the components of the magnetic moment of the material to be determined using the relationship $g = 2(1 + \varepsilon)$. For these three elemental ferromagnets the ratios $\varepsilon(\text{Fe}) = 0.05$, $\varepsilon(\text{Co}) = 0.09$, and $\varepsilon(\text{Ni}) = 0.105$ are

obtained. Since in these metallic ferromagnets the alternating field $H_{\mu\text{wave}}$ penetrates the material only to within the skin depth $\delta$ at the surface, defined in Eq. (W17.16), surface preparation is very important.

Additional parameters that can be obtained from measurements of $\omega_r$ in ferromagnets and ferrimagnets are the magnitudes of the effective anisotropy field $H_K$ and the effective molecular field $H_{\text{eff}}$. For example, the resonant frequency due to magnetic anisotropy effects alone is obtained when $H = 0$ and $H_{\text{tot}} = H_a$ in Eq. (W17.18). With $H_K = 2K/\mu_0 M_s$, measurement of $\omega_r = g\mu_0 H_K$ can yield $K$ if $M_s$ is known from independent measurements.

In antiferromagnets it is possible for the magnetizations of the two spin sublattices to precess at the same frequency. For a uniaxial antiferromagnet in zero applied magnetic field, the resonant frequency is

$$\omega_r = \gamma\mu_0 \sqrt{H_K(H_K + 2H_{\text{eff}})}, \tag{W17.19}$$

where $H_K$ is the effective anisotropy field and $H_{\text{eff}}$ is the effective molecular field. Values of $H_K$ and $H_{\text{eff}}$ obtained for the antiferromagnet $MnF_2$ via antiferromagnetic resonance are 700 and 43,000 kA/m, respectively.

For ferrimagnets the resonance occurs in essentially the same way as in ferromagnets as long as $H_{\text{eff}} \gg H$ or $H_K$. The resonant frequency can lie in the range from microwave to infrared frequencies, depending on the particular mode excited.

***Magnetic Relaxation.*** The time-dependent changes in the magnetization $M$ which lag behind changes in an applied magnetic field $H$ are known either as *magnetic relaxation* or as the *magnetic aftereffect*. Eddy currents can also lead to relaxation effects and have already been discussed. These magnetic relaxation effects can be reversible as long as no irreversible changes in the magnetic microstructure have occurred due to diffusion or to macroscopic structural changes.

Following a discontinuous change in $H$, changes in $M$ can exhibit exponential time dependencies expressed either by

$$M(t) = M_0(1 - e^{-t/\tau}) \tag{W17.20a}$$

or by

$$M(t) = M_0 e^{-t/\tau}, \tag{W17.20b}$$

where $\tau$ is the time constant for the relaxation process. The mathematical formalism for the description of magnetic relaxation is similar to that employed in Chapter W10 for a description of the anelastic mechanical properties of materials. The energy losses associated with periodic magnetic-relaxation processes typically occur at frequencies $\omega = 2\pi/\tau$, which are lower than those associated with ferromagnetic resonance. The characteristic time $\tau$ for magnetic relaxation depends on the nature of the microscopic processes controlling the relaxation process. The lifetime $\tau$ can be temperature dependent if the process is thermally activated. Examples of such processes include diffusion of atoms or the hopping of electrons from atom to atom.

A physical mechanism for the magnetic relaxation observed in BCC $\alpha$-Fe was first proposed by Snoek.[†] The *Snoek effect* is also discussed in Chapter 10, where

[†] J. Snoek, *Physica*, VI, 591 (1939).

its influence on the elastic properties of $\alpha$-Fe is described. Relaxation of the elastic properties is proposed to be due to the redistribution of C or N atoms among the available interstitial sites in the BCC crystal structure. The same redistribution of C or N affects the magnetization of the material through the magnetoelastic interaction and so is related to the magnetostriction of $\alpha$-Fe. An alternative explanation for the origin of the observed magnetic relaxation as suggested by Néel involves the effect on the anisotropic exchange interaction between Fe atoms due to the intervening interstitial C or N atoms.

Relaxation of the magnetization can also result from the thermally activated rotations of the magnetic moments of magnetic domains, of magnetic particles, or even of individual spins over energy barriers, which can be due, for example, to the effects of magnetic anisotropy. In small magnetic particles this effect is closely related to superparamagnetism. In the amorphous magnetic materials known as *spin glasses*, relaxation of the remanent magnetization occurs via the activation of single spins or clusters of strongly interacting spins over local energy barriers so that their magnetic moments point in energetically favorable directions. There is often a broad distribution of time constants associated with these processes so that the "freezing" process does not follow a simple thermal-activation law with a single time constant or activation energy. This process of spin glass "freezing" occurs over a wide range of temperatures.

The term *magnetic viscosity* is often used to describe the magnetic relaxation of collections of small magnetic particles or of spin glasses, for which there can exist a wide distribution of relaxation times resulting from a corresponding broad distribution of energy barriers to magnetization rotation, domain wall motion, and so on. In this case, the time dependence of the magnetization is often approximated by

$$M(t) = M_0 - S \ln(t/\tau_0), \tag{W17.21}$$

where $M_0$ and $\tau_0$ are constants and $S = -dM/d(\ln t)$ is the magnetic viscosity. There are good reasons, however, to avoid the use of this simple logarithmic time dependence for $M(t)$ because such an expression does not in general fit experimental observations at times that are either short or long compared to the time duration $t_{\text{exp}}$ of the measurement (Aharoni, 1996, pp. 100–105). Relaxation processes for which $\tau \ll t_{\text{exp}}$ or $\tau \gg t_{\text{exp}}$ will clearly fall outside the range of validity of Eq. (W17.21).

In many materials the magnetic viscosity levels off to a constant value at low temperatures, a result that is contrary to what is expected from thermally activated processes. This effect has been attributed to the quantum-mechanical reversal of the magnetization (i.e., to quantum tunneling of the magnetization).

***Magnetomechanical Damping.*** The energy losses associated with mechanical vibrations in magnetic materials, referred to as *magnetomechanical damping*, are generally larger than those observed in nonmagnetic materials. The stresses causing the vibrations in a magnetic material lead to strains, which in turn cause changes in the magnetization via magnetostriction. The result is that by Faraday's law, oscillatory stresses can result in the generation of eddy currents with their associated losses in a magnetic material. Losses due to domain wall motion can also result from applied stresses.

**TABLE W17.2 Technologically Important Magnetic Materials**

| Material | Magnetically Hard or Soft | Applications |
|---|---|---|
| Metals | | |
| Steels (alloyed with W, Cr, etc.) | Hard | Permanent magnets |
| Fe particles (oxide-coated) | Hard | Magnetic recording media |
| $Fe_xNi_{1-x}$ alloys: 78 Permalloy, $Fe_{0.22}Ni_{0.78}$; Supermalloy, $Fe_{0.16}Ni_{0.79}Mo_{0.05}$; Invar, $Fe_{0.65}Ni_{0.35}$ | Soft | Electromagnetic devices, magnetic recording heads, precision instruments |
| Mumetal: $\approx Fe_{0.18}Ni_{0.77}Cu_{0.05}$ | Soft | Magnetic shielding, transformer cores |
| Co alloys (CoCr, etc.) | Hard | Magnetic recording media |
| $Fe_{1-x}Si_x$ | Soft | Transformer cores |
| Fe:Si:Al alloys: Sendust,[a] 85Fe10Si5Al | Soft | Magnetic recording heads |
| Alnico alloys: Alnico 5,[a] 51Fe14Ni8Al24Co3Cu | Hard | Permanent magnets |
| Amorphous rare earth–transition metal alloys | Soft | Magneto-optical recording media |
| Amorphous Fe:B:Si:C alloys | Soft | Magnetostrictive elements |
| Intermetallic compounds | | |
| $SmCo_5$ and $Sm_2Co_{17}$ | Hard | Permanent magnets |
| $Nd_2Fe_{14}B$ | Hard | Permanent magnets |
| $TbFe_2$ and $(Tb_{0.3}Dy_{0.7})Fe_2$ (Terfenol-D) | Soft | Magnetostrictive elements |
| Ceramic compounds | | |
| $\gamma$-$Fe_2O_3$ | Hard | Magnetic recording media |
| $CrO_2$ | Hard | Magnetic recording media |
| $Mn_{1-x}Zn_xFe_2O_4$ | Soft | Magnetic recording heads |
| $Y_3Fe_5O_{12}$ (YIG) | Soft | Microwave technology |
| $BaO{\cdot}6Fe_2O_3$ or $SrO{\cdot}6Fe_2O_3$ ($BaFe_{12}O_{19}$, $SrFe_{12}O_{19}$) | Hard | Permanent magnets, magnetic recording media |

[a]Composition given in weight percent.

## W17.7 Technologically Important Magnetic Materials

See Table W17.2 for magnetic materials described in Chapters 17 and W17.

## W17.8 Details on Permanent-Magnet Materials

To illustrate the operation of a permanent magnet, consider a toroidal magnet producing a magnetic field $H_g$ in an airgap, as shown schematically in Fig. W17.6*a*. The introduction of the air gap leads to the presence of a demagnetizing field $\mathbf{H}_D = -N\mathbf{M}$ inside the magnet, directed opposite to both $\mathbf{M}$ and $\mathbf{B}$. When no external field $\mathbf{H}$ is applied to the magnet, its operating point will lie somewhere on the portion of the $B$–$H$ or $M$–$H$ loop in the second quadrant.

The portion of the $B$–$H$ loop in the second quadrant which determines the operation of a permanent magnet is the *demagnetization curve*, shown in Fig. W17.6*b*. Note that

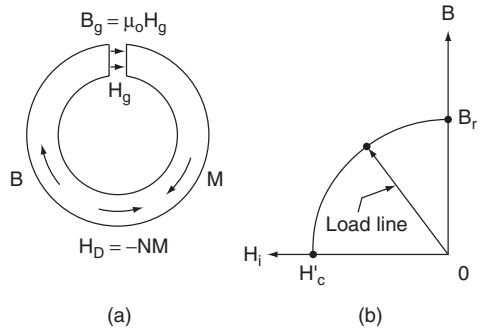


**Figure W17.6.** Permanent magnet: (*a*) configuration of a toroidal permanent magnet supplying a magnetic field $H_g$ to an air gap; (*b*) portion of the $B$–$H$ loop that determines operation of the permanent magnet, which is the demagnetization curve in the second quadrant.

it is standard practice to plot $B$–$H$ curves for permanent-magnet materials rather than the usual $M$–$H$ magnetization curves. Here the magnetic induction $\mathbf{B} = \mu_0(\mathbf{H}_i + \mathbf{M})$ in the material is shown plotted versus the internal magnetic field $\mathbf{H}_i$. The demagnetization curve extends from the remanent induction $B_r = \mu_0 M_r$ at $H_i = 0$ down to $H_i = -H'_c$, the coercive field corresponding to $B = 0$. Note that $B_r$ is the maximum flux density that the magnet can produce under closed-circuit conditions (i.e., in the absence of an air gap). The operating point for the magnet in the absence of an external magnetic field is determined by the presence of the air gap and the resulting demagnetizing field $\mathbf{H}_D$. In this case the internal magnetic field is given by

$$\mathbf{H}_i = \mathbf{H}_D = -N\mathbf{M}. \tag{W17.22}$$

The operating point is thus not at $B_r$ but rather, at the point where the magnetic induction $B(< B_r)$ is given by

$$\mathbf{B} = \mu_0(\mathbf{H}_D + \mathbf{M}) = \mu_0(1 - N)\mathbf{M}. \tag{W17.23}$$

Here $1 \geq N \geq 0$ is the demagnetizing factor for the magnet with the air gap. The magnetization $M$ is less than $M_r$, due to the presence of $\mathbf{H}_D$. Note that in the air gap $B_g = \mu_0 H_g \approx B$ if the gap is narrow enough so that the fringing magnetic fields are small.

For a given amount or volume of magnetic material, the highest field $H_g$ in a given air gap is achieved when the *energy density product* $(BH)$ of the magnetic induction $B$ and the field $H_i$ inside the magnet is maximized. The energy density product is also known as the *strength* of the magnet. The operating point of the magnet should therefore lie as close as possible to the point on the $B$–$H$ curve for which $(BH)$ is largest [i.e., at $(BH)_{\max}$]. The actual energy stored per unit volume is $BH/2$. In this way the permanent magnet needed to produce a given magnetic field can be as small as possible.

The actual point of operation of the permanent magnet is determined by the demagnetizing factor $N$ of the magnet with the air gap and corresponds to the magnetic induction given in Eq. (W17.23). The slope of the line connecting the origin to the operating point on the $B$–$H$ curve is therefore

$$s = \frac{B}{H_{\text{int}}} = \frac{-\mu_0(1 - N)}{N}. \tag{W17.24}$$

This is the *load line* of the magnet as shown in Fig. W17.6. Slopes of $s = \infty$ and $s = 0$ correspond, respectively, to the limiting values of $N = 0$ and $N = 1$. For $N \ll 1$, the slope is given approximately by $s = -\mu_0/N$.

***Transition Metal Alloys.*** The ferromagnetic $3d$ transition metals Fe, Co, and Ni are present in essentially all of the widely used permanent-magnet materials listed in Table W17.3, either in alloys with each other or with other transition metals, in intermetallic compounds with rare earth metals, or in ceramic compounds. The magnetic anisotropy field $H_K$ for pure Fe is only $\approx 40$ kA/m, which eliminates pure Fe as a material for most permanent-magnet applications due to its relatively low coercive field $H_c$. The precipitation-hardened alloys based primarily on Fe, Ni, Al, and Co, as well as some steels that have permanent-magnet applications, are discussed next.

*Precipitation-Hardened Alloys.* *Precipitation hardening* in the case of magnetic materials refers to the use of heat treatments to enhance the magnetic hardness of the material by the precipitation of a second phase which can pin domain walls and hence increase $H_c$. By varying both the specific processing treatments employed and the composition, the alloys known in the United States as Alnico and based on Fe, Al, Ni, Co, and so on, can be prepared with magnetic properties, which have led to their widespread use in permanent magnets. Many other transition metal alloys based on Fe, Co, or Ni can also undergo precipitation hardening for use in permanent magnets.

**TABLE W17.3 Properties of Permanent-Magnet Materials**

| Material | $(BH)_{\max}$ (kJ/m$^3$)[a] | $B_r$ (T) | $H_c'$[b] (kA/m) | $T_C$ (K) |
|---|---|---|---|---|
| Transition Metal Alloys | | | | |
| Alnico 5[c]: (51Fe, 14Ni, 8Al, 24Co, 3Cu) | 35.8 | 1.25 | 43.8 | 1120 |
| Steels[c] | | | | |
| Cobalt steel (35Co, 0.7C, 4Cr, 5W, bal. Fe) | 7.7 | 0.95 | 19.1 | |
| Tungsten steel (5W, 0.3Mn, 0.7C, bal. Fe) | 2.5 | 1.03 | 5.6 | |
| Rare Earth–Transition Metal Intermetallic Compounds | | | | |
| Nd–Fe–B[d] | 200–380 | 1.0–1.4 | 700–1000 | 580 |
| $SmCo_5$[e] | 130–180 | 0.8–0.9 | 600–670 | 990 |
| $Sm(Co,Fe,Cu,Zr)_7$[e] | 200–240 | 0.95–1.15 | 600–900 | 1070 |
| Ceramics | | | | |
| $BaO{\cdot}6Fe_2O_3$[d] | 28 | 0.4 | 250 | 720 |

[a]Note that 1 kJ/m$^3$ = 1 kA·T/m.
[b]The quantity $H_c'$ is the coercive field corresponding to $B = 0$.
[c]Data from D. R. Lide and H. P. R. Frederikse, eds., *CRC Handbook of Chemistry and Physics*, CRC Press, Boca Raton, Fla., 1994, pp. 12–113. The alloy composition is given in weight percent. See the Handbook for methods of fabrication.
[d]Commercial material from Magnet Sales & Manufacturing Catalog.
[e]Data from K. H. J. Buschow, *Rep. Prog. Phys.*, **54**, 1123 (1991). $Sm(Co,Fe,Cu,Zr)_7$ is a two-phase material which can be thought of as a composite of $SmCo_5$- and $Sm_2Co_{17}$-type phases.

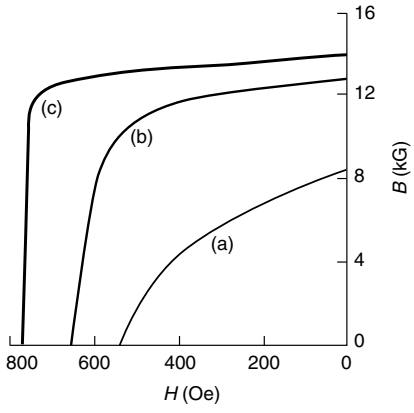


**Figure W17.7.** Demagnetization curves of an Alnico alloy, 51.8Fe, 7.5Al, 23Co, 3Cu, 0.7Nb in wt %, cooled from $T = 1250°C$ and annealed at $T = 560$ to 590°C: (*a*) randomly oriented grains with no heat treatment in a magnetic field; $(BH)_{max} = 14$ kJ/m$^3$; (*b*) randomly oriented grains heat-treated in a magnetic field; $(BH)_{max} = 43$ kJ/m$^3$; (*c*) columnar grains heat-treated in a magnetic field; $(BH)_{max} = 69$ kJ/m$^3$. [From J. E. Gould, *Proc. I.E.E.*, **106A**, 493 (1959). Copyright 1959, IEE Publishing.]

A typical precipitation-hardened alloy is Alnico 5, which has the composition (in weight percent) 51Fe, 14Ni, 8Al, 24Co, and 3Cu. The extrinsic magnetic properties of Alnico 5 are listed in Table W17.3. Due to their high $T_C$ values of $\approx 1120$ K, Alnico 5 and similar alloys have higher maximum operating temperatures than most other permanent magnets. Following quenching from $T \approx 1200°C$ and annealing in the range 500 to 600°C, these alloys consist of highly magnetic rodlike particles of $\alpha$-Fe embedded in a weakly magnetic matrix of Ni and Al. When cooled slowly from $T = 1200°C$ to below $T_C$ in a magnetic field, the precipitation occurs in such a way that the long axes of the particles become aligned with each other, thus increasing the shape magnetic anisotropy of the material and its coercive field. This is illustrated in Fig. W17.7, where the demagnetization curves for an Alnico alloy are shown following three different types of thermomagnetic treatment.

Alnico alloys have high values of $B_r$, due to their high Fe contents but have lower coercive fields $H_c$ compared to the other permanent-magnet materials listed in Table W17.3. The magnitude of the coercive fields of Alnico alloys can be attributed to the pronounced shape anisotropy of the magnetic particles. The maximum magnetic anisotropy attainable in these alloys is determined by the difference $(N_\perp - N_\parallel)$ of the demagnetization coefficients of the particles [see Eq. (17.16)]. Even better magnetic properties [i.e., higher $B_r$, $(BH)_{max}$, and $H'_c$] can be found in highly [100]-oriented alloys with columnar microstructure obtained by controlled solidification from the melt.

Co is apparently required for the appearance of significant magnetic anisotropy in these alloys, while additions of Nb and Ti can also lead to increased values of $H'_c$. The physical reasons for these changes are not clear.

*Steels.* Steels alloyed with W, Cr, and Co have been used extensively as permanent magnets. Given the proper heat treatment, these alloying elements can react with the C in the steel, forming precipitates of carbides of W, Cr, and Co which act to impede the motion of domain walls. Anisotropy effects associated with the shapes of these carbide precipitates are apparently not as strong as in typical Alnico alloys, which

have coercive fields that are higher by a factor of 3 or more. The low values of $H_c$ in steels limit their attainable values of $(BH)_{\max}$.

The martensitic lattice transformations from the FCC $\gamma$-phase to the BCC $\alpha$-phase that occur in these steels upon cooling lead to lattice distortions due to the resulting high internal stresses. The magnetic anisotropy of magnet steels is therefore enhanced by stress-related magnetostrictive effects.

***Rare Earth–Transition Metal Intermetallic Compounds.*** The most attractive materials for current high-performance permanent magnets are the intermetallic compounds based on rare earths and the ferromagnetic transition metals Fe and Co. These materials, sometimes referred to as *supermagnets*, possess the highest-known coercive fields, $H_c \approx 1100$ kA/m, and energy products, $(BH)_{\max} \approx 300$ kJ/m$^3$. The low-symmetry hexagonal or tetragonal crystal structures of these materials expose the rare earth ions to the high magnetocrystalline anisotropy needed for enhancing the coercive field. The transition metal components keep $T_C$ sufficiently high for practical applications. An important advantage of the rare earth–based permanent-magnet materials is that they can be used to generate the same magnetic fields as iron-core electromagnets, which are 10 times as massive. This feature has made possible miniaturized electrical motors and, in general, smaller and lighter electromagnetic devices and products. Larger magnetic inductions, in the range 3 to 10 T, require the use of superconducting magnets. The important intermetallic compounds $SmCo_5$, $Sm_2Co_{17}$, and $Nd_2Fe_{14}B$ are discussed next.

*$SmCo_5$ and $Sm_2Co_{17}$.* The first permanent-magnet materials, consisting of rare earth–transition metal (RE–TM) intermetallic compounds and based on Sm and Co, were discovered in the early 1960s. These materials have high values of $M_{\text{sat}}$, due to the ferromagnetic coupling of the Sm and Co spins. This is not found to be the case in alloys containing heavy rare earths, such as Gd, where the RE–TM coupling is antiferromagnetic. The substitution of other magnetic 3*d* transition metals, such as Fe, Mn, Cr, or Ni for Co, in these RE–TM compounds has not been successful, due to the resulting low $T_C$ values or low magnetic anisotropies. The high $T_C$ values of these alloys make them attractive for use in applications in which the operating temperature of the magnet is relatively high.

According to the Hume–Rothery rules described in Chapter 12, the fact that the RE ionic radii are much greater than those of the TM ions strongly limits the possibility of the formation of RE–TM solid solutions. Instead, a series of intermetallic compounds are formed. The crystal structure of $SmCo_5$ is hexagonal and that of $Sm_2Co_{17}$ is trigonal (rhombohedral) (Fig. W17.8). In the $SmCo_5$ structure the planes containing the Sm ions and twice as many Co ions lie between adjacent planes containing only Co atoms. The $Sm_2Co_{17}$ structure is derived from the $SmCo_5$ structure by an ordered replacement of one-third of the Sm ions by pairs ("dumbbells") of Co ions that are aligned along the *c* axis.

The overall magnetocrystalline anisotropies of both Sm–Co compounds is uniaxial, with $SmCo_5$ having the largest value observed for any magnetic material, corresponding to an effective magnetic anisotropy field $H_K \approx 3.2 \times 10^4$ kA/m. In the $Sm_2Co_{17}$ structure the dumbbell pairs of Co atoms prefer to have their magnetic moments lying in the basal plane, thereby reducing the overall magnetic anisotropy of the material.

Recently, Fe-based compounds such as $Sm_2Fe_{17}N_{3-x}$ have been developed with high $T_C$ values, up to 749 K, strong uniaxial anisotropy, and high saturation magnetization.

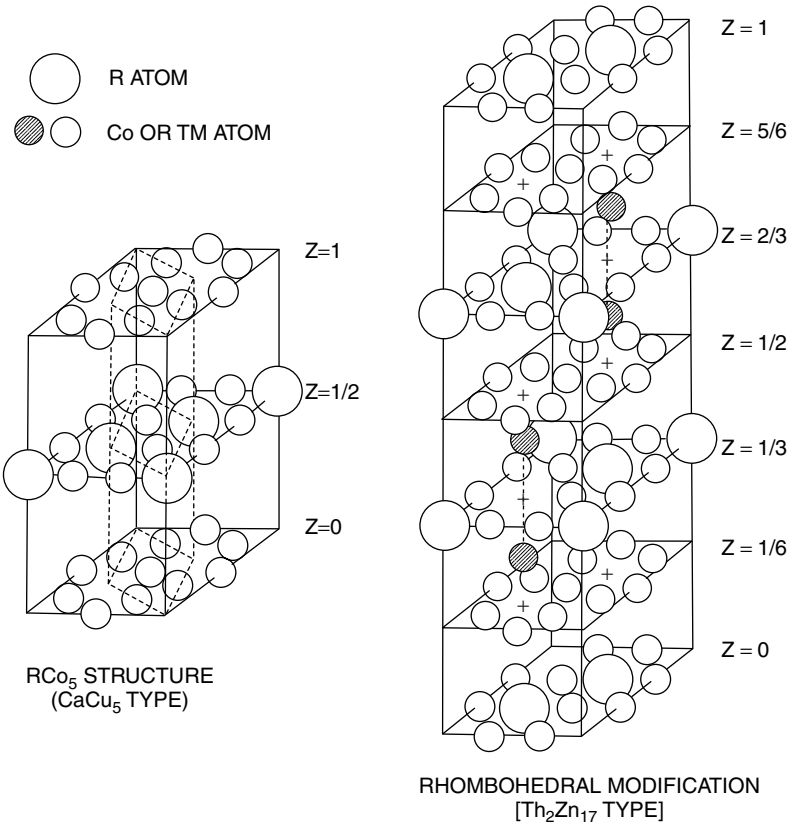


**Figure W17.8.** Crystal structures of the intermetallic compounds hexagonal $SmCo_5$ and rhombohedral $Sm_2Co_{17}$. The substituted "dumbbell" Co ions in $Sm_2Co_{17}$ appear crosshatched. (From K. Kumar, *J. Appl. Phys.*, **63**, R13 (1988). Copyright 1988 by the American Institute of Physics.)

The N atoms enter octahedral interstitial sites in the structure. In materials such as $Sm_2Fe_{15}Ga_2C_{3-x}$, C atoms can serve the same purpose. In addition, Ga has been substituted for some of the Fe in order to increase $T_C$ and the uniaxial anisotropy field. The presence of the interstitial N or C atoms expands the structure and apparently has the effect of strengthening the magnetism by supporting the formation of ferromagnetic networks of Fe atoms in these materials.

The best commercially available materials are precipitation-hardened composites consisting of a $Sm_2Co_{17}$-type phase embedded in a $SmCo_5$-type matrix. These materials combine the high $M_{sat}$ value of $Sm_2Co_{17}$ with the high magnetic hardness of $SmCo_5$. The high observed values of $H_c$ result from the alignment of the easy axes of the particles parallel to each other in the material. These composites have the approximate composition $SmCo_{7.7}$ and also typically contain some Fe, Cu, and Zr atoms replacing some of the Co.

Powder metallurgy techniques are used in the fabrication of these magnets. The elements are first melted together, then ground into micrometer-sized particles. The $c$ axes of the particles are aligned magnetically in a magnetic field. The particles are then densified by sintering. Finally, thermal treatments are utilized for the optimization of $H_c$.

*$Nd_2Fe_{14}B$.* The intermetallic compound $Nd_2Fe_{14}B$, discovered in 1984, exhibits the most desirable magnetic properties of all permanent-magnet materials at room temperature (see Table W17.3). Since it is based on Fe, $Nd_2Fe_{14}B$ has the advantage of being less expensive than the Co-based materials discussed earlier. In addition, $Nd^{3+}$ has a larger magnetic moment than $Sm^{3+}$ and couples ferromagnetically to the magnetic moments of the Fe atoms, leading to a higher magnetization. The magnetic coupling between the Nd $4f$ electrons and the Fe $3d$ electrons is believed to be indirect, occurring not via the RKKY interaction through the conduction electrons but instead, through the rare earth $5d$ electrons. The ion $Nd^{3+}$ has an outer electron configuration $4f^3$ and contributes one $5d$ and two $6s$ electrons to the conduction bands. The Fe magnetic moment is $\approx 2.1\mu_B$, close to the value found in pure $\alpha$-Fe.

$Nd_2Fe_{14}B$ has a complicated tetragonal unit cell with dimensions $a = 0.88$ nm and $c = 1.22$ nm and containing 68 atoms (i.e., four formula units). The crystal structure presented in Fig. W17.9 is essentially a layered one, with sheets of Nd and B atoms

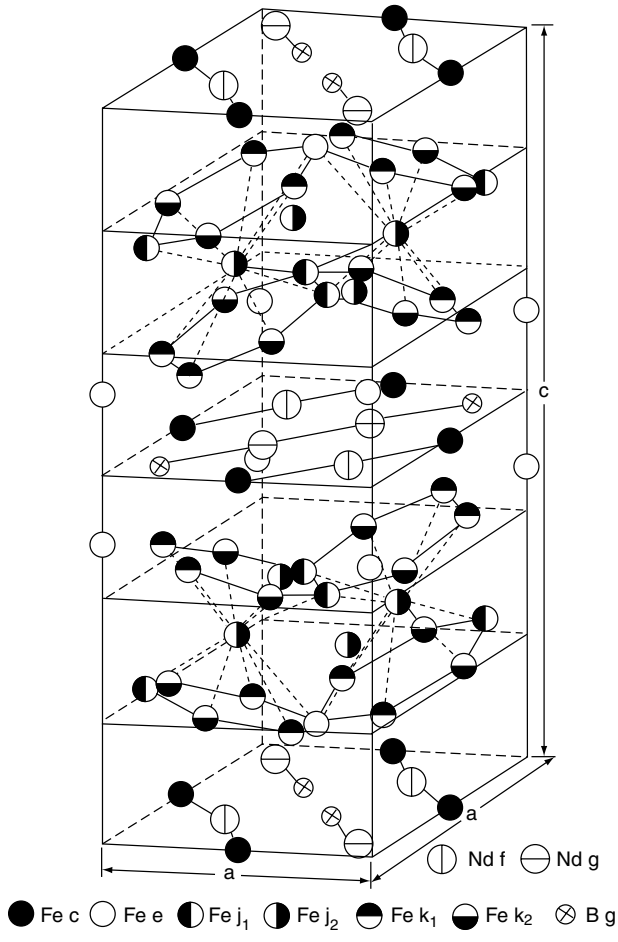


**Figure W17.9.** Tetragonal unit cell of $Nd_2Fe_{14}B$. The structure is essentially a layered one, with sheets of Nd and B atoms (and some Fe atoms) lying between close-packed double layers of Fe atoms. (From J. F. Herbst, *Rev. Mod. Phys.*, **63**, 819 (1991). Copyright 1991 by the American Physical Society.)

(and some Fe atoms) lying between close-packed double layers of Fe atoms. Six crystallographically distinct positions for the Fe atoms and two for the Nd atoms exist in this structure. The origin of the strong uniaxial magnetocrystalline anisotropy of $Nd_2Fe_{14}B$ is the low symmetry of the Nd sites and, apparently, the interaction of the $Nd^{3+}$ ions with the resulting strong crystal fields.

Despite the crystal-field effects, the $Nd^{3+}$ ions retain their full magnetic moment due to the strong on-site spin–orbit interaction (i.e., the orbital angular momentum **L** is not quenched). In this structure the Nd atoms lie within hexagonal prisms of Fe atoms while the B atoms lie within trigonal prisms of Fe atoms. These trigonal prisms are also a common and fundamental feature of transition metal–metalloid structures such as those found in the FeB and $Fe_3C$ systems. The role of the B in $Nd_2Fe_{14}B$ is to produce a low-symmetry crystal structure without causing an appreciable reduction of the magnetization of the material.

The material $Nd_2Fe_{14}B$ is a uniaxial ferromagnet with a fairly low $T_C$ value of 585 K and with the all Nd and Fe spins aligned at room temperature parallel to the $c$ axis, the easy axis for the magnetization **M**. The resulting saturation magnetization is quite high, $M_{\text{sat}} = 1270$ kA/m, even higher than the value 800 kA/m for $SmCo_5$. As a measure of the strength of the uniaxial magnetic anisotropy, the effective magnetic anisotropy field $H_K$ is about 7200 kA/m.

NdFeB magnet material can be formed by rapid solidification, (i.e., by melt spinning and quenching into ribbon form) or by the pressing and sintering of powder material. The ribbon material has a metastable microstructure that is very sensitive to the quenching rate. The optimum material consists of 20-nm grains of $Nd_2Fe_{14}B$ surrounded by an approximately 2-nm-thick amorphous intergranular phase. The grain boundaries pin the domain walls, thereby impeding their motion and increasing the coercive field. Processing is necessary to transform the brittle ribbon material into the final dense form, with the two-phase microstructure suitable for permanent-magnet applications.

Improvements in the properties of $Nd_2Fe_{14}B$ can be achieved by introducing a variety of alloying elements (e.g., substituting Co for some of the Fe atoms raises $T_C$, replacing some of the Nd by Dy or Gd atoms enhances the anisotropy, etc.). Currently used NdFeB magnet materials are based on $Nd_2Fe_{14}B$ but actually correspond to a range of compositions and microstructures.

***Ceramics.*** Permanent magnets based on the ceramic compounds barium ferrite, $BaO{\cdot}6Fe_2O_3$ ($BaFe_{12}O_{19}$), strontium ferrite, $SrO{\cdot}6Fe_2O_3$, and their solid solutions have the advantages of very high coercive fields, $H_c \approx 200$ kA/m, due to the strong uniaxial magnetocrystalline anisotropy field of this material, $H_K \approx 1300$ kA/m. They also possess high environmental stability, due to the absence of problems associated with oxidation. The magnetic properties depend critically on the sintering of the ceramic powders to obtain bulk material. The fact that $H_c$ is typically well below $H_K$ may be due to the platelet shape of the particles and the fact that the resulting shape anisotropy opposes the larger uniaxial magnetocrystalline anisotropy. This issue is also mentioned in Section W17.9, where the use of barium ferrite in magnetic recording media is discussed.

These ceramic materials are ferrimagnetic and thus have relatively low values of $B_r$ and $M_{\text{sat}}$. Their high values of $H_c$ and low cost have nevertheless led to widespread applications in permanent magnets and in magnetic recording media. Their high

resistivities, $\rho \approx 10^2$ to $10^7 \Omega \cdot m$, make them useful for high-frequency applications. The flexible magnets consisting of a magnetic powder such as barium ferrite bonded in a flexible binder are an interesting and ubiquitous application of these ceramic materials.

## W17.9 Details on Magnetic Recording Materials

***Particulate Magnetic Recording Media.*** The intrinsic shape anisotropy of small, elongated magnetic particles can be a convenient and stable source of magnetic anisotropy for controlling $H_c$. Particulate recording media therefore often consist of elongated magnetic particles dispersed and embedded (20 to 50% of total volume) in a suitable medium consisting of organic components (polymers or resins), which is then applied as a 0.2 to 10-μm-thick film to a nonmagnetic support (e.g., a tape or disk). For superior recording performance it is clearly desirable to have particles of a fixed length-to-width ratio as well as of a uniform size distribution. Some of the particulate magnetic materials currently used in recording media are discussed next.

*Iron Oxides.* The iron oxide $\gamma$-$Fe_2O_3$ (maghemite) was one of the first magnetic materials used for recording applications and is still in wide use today, due to its low cost and physical and chemical stability. Figure W17.10 illustrates a transmission electron micrograph of needle-shaped (acicular) particles of $\gamma$-$Fe_2O_3$. These magnetic particles are typically oriented with their long axis, which in this case is also the easy axis of magnetization due to shape anisotropy, parallel to the surface of the film and also parallel to the direction of the motion of the head along the film. In this longitudinal geometry the magnetic properties are optimized with high $M_r$ and with good magnetic squareness. The lengths of the particles are typically 0.2 to 0.4 μm.

Acicular iron oxide particles are magnetically stable since the shape-induced uniaxial magnetic anisotropy is unaffected by changes in temperature and stress, as opposed

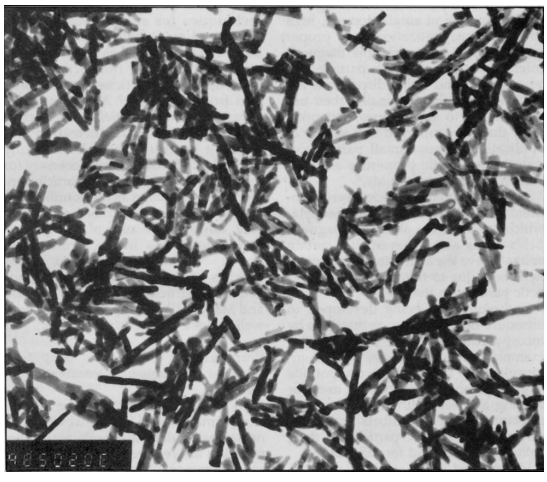

**Figure W17.10.** Needle-shaped (acicular) particles of $\gamma$-$Fe_2O_3$ (maghemite) used in magnetic recording media are shown in a transmission electron micrograph. The lengths of the particles are 0.2 to 0.4 μm and the aspect ratio is 7:10. (From M. Ozaki, *Mater. Res. Soc. Bull.*, **14**(12), 35 (1989).)

to magnetocrystalline anisotropy, which is often quite sensitive to such changes. The chemical stability of the $\gamma$-$Fe_2O_3$ particles is due in large part to the fact that they are fully oxidized.

The oxide $\gamma$-$Fe_2O_3$ is a ferrimagnet with the cubic inverse spinel crystal structure in which there are vacancies on one-sixth of the normally occupied octahedral $Fe^{3+}$ sites of the $Fe_3O_4$ inverse spinel crystal structure, described in Section 9.8. The remaining octahedral sites that would normally be occupied by $Fe^{2+}$ in $Fe_3O_4$ are occupied by $Fe^{3+}$ instead. Due to the partial cancellation of the sublattice magnetizations, the value of $M_{\text{sat}} \approx 400$ kA/m for $\gamma$-$Fe_2O_3$ is well below the corresponding value of 1710 kA/m for pure Fe at $T = 300$ K. The small particles used in recording typically have $M_{\text{sat}} \approx$ 350 kA/m, due to the presence of magnetically inactive surface layers or other defects.

The values of $H_c$ observed for the $\gamma$-$Fe_2O_3$ particles are in the range 24 to 32 kA/m. These are an order of magnitude below the estimate given in Table W17.1 for the case of a magnetic field applied parallel to the long axis of a needle-shaped magnetic particle (i.e., $H_c = H_K \approx N_\perp M_s = 0.5 M_s$). This estimate for $H_c$ corresponds to the reversal of the magnetization by coherent rotation of **M**. In practice the magnetization rotates incoherently (i.e., it begins to reverse direction at much lower fields) due to the fact that the magnetization directions in different parts of the sample do not remain parallel in ways that are influenced by defects or inhomogeneities in the particles.

*$CrO_2$.* Needle-shaped particles of the tetragonal transition metal oxide $CrO_2$ have also found applications in magnetic recording due to their higher coercive fields, in the range 44 to 48 kA/m. The oxide $CrO_2$ is unique because it is the only transition metal oxide that is ferromagnetic at room temperature. Greater recording densities are possible with $CrO_2$ since the higher values of $H_c$ make it possible to overcome the effects of the larger demagnetizing fields $H_D$ which occur as the recording density increases. The high coercive fields that are observed result from both the shape and magnetocrystalline anisotropies of the $CrO_2$ particles.

*Iron Oxides Containing Co.* The most widely used particulate recording media now employ iron oxide particles whose coercive fields have been enhanced by the addition of cobalt ($Co^{2+}$). For these cobalt-modified iron oxide particles $H_c$ is typically in the range 32 to 80 kA/m. These materials also allow higher recording densities than do the pure iron oxides discussed earlier. The enhancement of $H_c$ resulting from the addition of Co to the iron oxide structure is due to the increase in the magnetocrystalline anisotropy of the material when $Co^{2+}$ ions experience the octahedral crystal fields of the surrounding $O^{2-}$ ions. Exchange interactions with the next-NN $Fe^{3+}$ ions also contribute to the enhanced anisotropy.

The current practice is to apply Co only to the surfaces of the iron oxide particles. These surface-modified particles show better stability with the Co surface layer enhancing the uniaxial anisotropy and coercive force of the particles.

*Metal Particles.* Small, needle-shaped particles of ferromagnetic Fe coated with surface oxides for passivation are advantageous for high-density recording because they have higher magnetizations and coercive fields than those of the ferrimagnetic or ferromagnetic oxide particles discussed earlier. While pure Fe has a spontaneous magnetization $M_s = 1710$ kA/m at $T = 300$ K, these Fe particles, which are about 200 nm long and only 20 nm in diameter, have effective values of $M_s \approx$

750–900 kA/m, due to the surface oxides, which can occupy about one-half of the particle volume. These reduced values of $M_s$ are still nearly twice as large as those found for oxide particles. Typical values of $H_c$ are 120 kA/m, also well above the values of $H_c$ for oxide particles. Since the uniaxial magnetic anisotropy of these Fe particles is due to their elongated shape, their coercive fields show little dependence on temperature or stress.

*Barium Ferrite.* The ferrimagnetic material barium ferrite, $BaO{\cdot}6Fe_2O_3$ ($BaFe_{12}O_{19}$), is unique among recording materials, due to its very high magnetocrystalline anisotropy and hence $H_c$ in the low-symmetry hexagonal *magnetoplumbite* crystal structure. This crystal structure has a unit cell consisting of two formula units and containing two spinel-like regions, each with the formula $Fe_6O_8$, and two HCP-like regions, each with the formula $BaFe_6O_{11}$, in which an oxygen atom in a close-packed layer is replaced by a $Ba^{2+}$ ion. The crystal structure of $BaFe_{12}O_{19}$ is illustrated in Fig. W17.11, where one half of the hexagonal unit cell is shown. The other half is obtained by a mirror reflection relative to either the top or the bottom plane. The high intrinsic $H_c$ value, 160 to 240 kA/m, of this material is combined, however, with a rather low $M_{\text{sat}}$ value of $\approx 300$ kA/m. Although barium ferrite particles have the shape of thin hexagonal platelets (Fig. W17.12), the easy direction of magnetization remains along the $c$ axis, which is perpendicular to the plates. This results from the dominance of the magnetocrystalline anisotropy over the shape anisotropy. A perpendicular rather than a longitudinal recording medium results when the barium ferrite platelets are present with their surfaces parallel to the surface of the medium.

The intrinsic coercive field of barium ferrite is actually too high for magnetic recording applications (but not for the permanent-magnet applications discussed earlier), and is usually reduced to $\approx 4$ to 10 kA/m by the replacement of some of the $Fe^{3+}$ ions by less magnetic $Co^{2+}$ ions or by nonmagnetic $Ti^{4+}$ ions.

***Thin-Film Magnetic Recording Media.*** In addition to the composite particulate magnetic recording media just described, continuous magnetic thin films are the material of choice for hard-disk applications, due in large part to their potential for higher

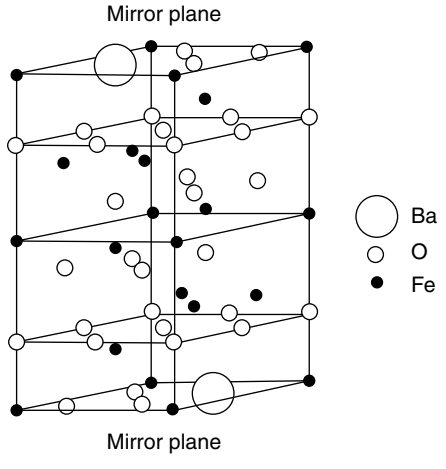


**Figure W17.11.** Crystal structure of $BaFe_{12}O_{19}$ with one half of the hexagonal unit cell shown.

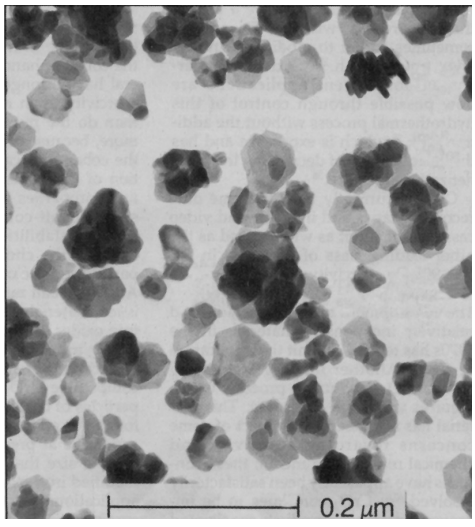


**Figure W17.12.** Thin platelet-shaped hexagonal particles of barium ferrite, $BaFe_{12}O_{19}$. (From M. P. Sharrock, *Mater. Res. Soc. Bull.*, **15**(3), 53 (1990).)

recording densities than are currently possible in particulate media. The higher densities arise from the higher coercive fields and remanent magnetizations possible in magnetic alloy films. Another advantage is that the magnetic properties of thin films can readily be controlled by varying the composition and the deposition and processing conditions. A significant disadvantage of thin-film media is that they are much less durable than currently used particulate media.

The criteria for continuous thin-film recording media are essentially the same as those for particulate media (i.e., magnetic hardness), with high $H_c$, high $M_r$, high coercivity squareness, and low noise. As a result, it is important to control the magnitudes and distributions of the crystalline, shape, and stress anisotropies in thin-film magnetic recording media. Typical thin-film media with thicknesses in the range 10 to 100 nm have values of $M_s$ in the range 5 to 100 kA/m and $H_c$ in the range 40 to 120 kA/m.

The ideal thin-film recording medium should consist of small (10 to 50 nm) magnetically noninteracting crystallites or grains, with as uniform a size distribution as possible. The grains should not be too small or superparamagnetic effects will limit the stability of information storage. The actual magnetic behavior of thin-film recording media can be complicated, as it depends on the interactions between the grains and on the magnetic anisotropy energies, which in turn depend on internal stresses, composition gradients, and properties of the grain boundaries.

The thin films used in longitudinal recording media typically include the ferromagnet Co along with other transition metals, such as Ni, Cr, Ta, Pt, Re, and Zr. A wide range of polycrystalline Co-based alloy films has been prepared via electrochemical deposition and by physical processes such as evaporation and sputtering. A tilted columnar grain structure with strong shape anisotropy is obtained by evaporating the films at an angle of 70° from the normal. The voids that appear between the columnar grains are beneficial because they help to isolate the grains physically and magnetically, thereby reducing noise in the recording. These metal-evaporated tape (MET) media

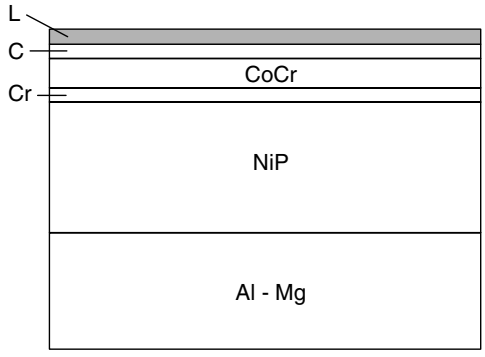


**Figure W17.13.** Schematic cross section of a magnetic hard disk. Typical thicknesses of the layers are as follows: Al–Mg, 0.6 to 0.8 mm; NiP, 10 μm; Cr, 20 to 100 nm; CoCr, 30 nm; a-C, 10 to 20 nm; L, lubricant, several monolayers. [Adapted from K. E. Johnson et al., *IBM J. Res. Dev.*, **40**, 511 (1996).]

based on Co, CoNi, or CoNiCr can have high coercive fields of 120 kA/m. The wear and corrosion resistance of the films can be enhanced by a surface Co oxide when they are deposited in the presence of oxygen. The desired magnetic isolation of the grains is also improved by the presence of the surface oxide.

The cross section of a typical thin-film magnetic hard disk is illustrated in Fig. W17.13. The mechanical support for the multiple coatings that are utilized is an Al–Mg alloy disk. The disk is plated with an amorphous layer of NiP, which is then textured with grooves to improve the wear characteristics of the disk. The active layer is typically a ferromagnetic film of CoCr containing additional elements, such as Pt and Ta, which control its coercivity. The CoCr-based film consists of magnetic domains that are readily alignable by the applied magnetic field of the write head. It is covered by a protective, hard amorphous carbon (a-C) layer, which in turn is coated with a polymeric lubricant to reduce friction. The CoCr active layer is deposited on an underlayer of Cr, which enhances the deposition of the active layer with high $H_c$ and with its easy axis of magnetization in-plane. The flatness of the outer a-C layer is of paramount importance, since the disk rotates past the read/write head at a speed of about 40 m/s and at a distance of only about 100 nm.

Compositional segregation in the CoCr-based layer can help to minimize intergrain interactions, leading to lower noise. Alloy compositions can be chosen that will undergo a phase change or spinodal decomposition at elevated temperatures to achieve the desired segregation.

Ferromagnetic thin films have also been developed for perpendicular recording applications and have great potential for higher bit densities. Sputtered CoCr alloy films with columnar microstructure can show perpendicular magnetic anisotropy, due to the orientation of the $c$ axis of the grains perpendicular to the plane of the film. The complicated dependencies of the magnetic, structural, and mechanical properties of the films on the deposition conditions present both a considerable challenge and the flexibility needed to prepare films with the characteristics desired. One current approach involves deposition of these Co-based films onto Cr underlying films, which help to enhance the coercive field of the film deposited. This example of the use of surfaces and interfaces to modify the equilibrium bulk properties of magnetic films is typical of

processes that will play an increasingly important role in the continuing development of higher-density, lower-noise magnetic recording media.

## W17.10 Details on Magneto-Optical Recording Materials

The magnetic materials currently in use in MO recording media that so far have the best combination of magnetic and MO properties are amorphous alloys of rare earths and transition metals (i.e., RE–TM alloy media) in which the RE ions interact antiferromagnetically with the TM ions. The magnetization of the RE ions dominates at low temperatures, while at higher temperature the magnetization of the TM ions dominates. At an intermediate temperature, known as the *compensation temperature* $T_{\text{comp}}$, the RE and TM magnetizations cancel each other. The temperature $T_{\text{comp}}$ can be adjusted by varying the film composition or the deposition and processing conditions.

Examples of amorphous RE–TM alloys include the ternary alloys a-GdTbFe, a-TbFeCo, and a-DyFeCo, which have the required magnetic and MO properties but which have limited chemical stability. Although the source of the perpendicular magnetic anisotropy observed in these amorphous alloy films is not clear, possibilities include stress-induced anisotropy, pair ordering, and single-ion anisotropy. Shape-induced magnetic anistropy in thin films favors an easy axis in the plane of the film (i.e., parallel or longitudinal anisotropy). Typical values of the anisotropy coefficients are $K_u = 10^4$ and $10^5$ J/m$^3$ for the Gd- and Tb-based alloys, respectively.

Figure W17.14 presents a useful summary of the magnetization $M_s$, coercive field $H_c$, uniaxial anisotropy coefficient $K_u$, and Kerr rotation $\theta_K$ of an a-$Gd_{24}Tb_1Fe_{75}$ alloy from low temperatures up to its $T_C$, which is just above 500 K. For this alloy the compensation temperature $T_{\text{comp}}$ at which the sublattices of the antiferromagnetically coupled Gd and Fe magnetic moments cancel each other is close to 340 K (i.e., near the typical operating temperature). At $T_{\text{comp}}$ the coercive field $H_c$ diverges as $M_s \to 0$ (see Table W17.1). When the magnetization $\mathbf{M}_s$ of a magnetic domain is very low, due

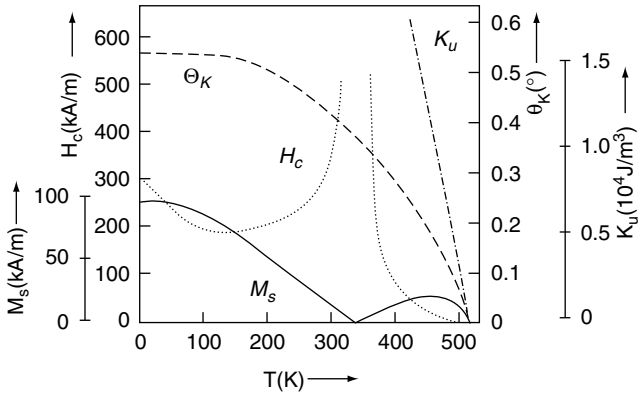


**Figure W17.14.** Magnetization $M_s$, coercive field $H_c$, uniaxial anisotropy coefficient $K_u$, and Kerr rotation $\theta_K$ for an amorphous $Gd_{24}Tb_1Fe_{75}$ alloy from low temperatures up to its $T_C$. The compensation temperature $T_{\text{comp}}$ at which the sublattices of Gd magnetic moments and Fe magnetic moments cancel each other is close to 340 K. (From F. J. A. M. Greidanus and W. B. Zeper, *Mater. Res. Soc. Bull.*, **15**(4), 31 (1990).)

to the compensation effect, very high external fields are required to exert large enough torques to rotate $\mathbf{M}_s$. Thus the $H_c$ required becomes very large in the vicinity of $T_{\text{comp}}$. The Kerr rotation is determined primarily by the Fe spins since the Kerr effect for the RE elements is small.

The intrinsic magnetic properties of these amorphous RE–TM alloys are determined by their compositions and can be controlled by varying the Fe/Co ratio in a-TbFeCo alloys and the Gd/Fe ratio in a-GdTbFe alloys. Film microstructure also plays a critical role in these alloys and is determined by the deposition and processing conditions. The absence of grain boundaries aids in the reduction of noise. The main difficulty with amorphous RE–TM films is their lack of chemical stability.

Promising MO materials for future applications include oxides such as ferrites and garnets and Co/Pt multilayers, all of which can have good chemical stability. In the Co/Pt multilayers the perpendicular magnetic anisotropy may arise from interactions at the interfaces between the Co and the Pt layers.

## W17.11 Details on Fe Alloys and Electrical Steels

***Pure Fe and Fe–Ni Alloys.*** The magnetic properties of pure Fe are discussed first as the classic example of a magnetically soft material. As Fe is treated to remove impurities such as C, N, O, and S (typically, by heating in $H_2$ or in $H_2$ and $H_2O$), the permeability $\mu$ increases dramatically, $H_c$ decreases steadily, and $M_s$ is hardly affected. In addition, the hysteresis loop narrows considerably and eddy current and other magnetic losses due to irreversible processes are reduced. This behavior is illustrated in Table W17.4 for two grades of Fe and reflects the fact that $M_s$ is an intrinsic property, while $\mu$ and $H_c$ are extrinsic, depending on microstructure, impurity content, and so on. Since the impurities listed earlier have limited solubilities in Fe, $\approx 0.01$ at %, they tend to form inclusions or precipitates such as $Fe_3C$, $Fe_4N$, FeO, and FeS. These precipitates, if present, impede or pin the motion of domain walls. Their elimination thus allows domain walls to move more readily.

**TABLE W17.4 Magnetic Properties of Pure Fe and Some Magnetically Soft Fe Alloys and Electrical Steels at Room Temperature**

| Alloy[a] | $\mu_r$(max)[b] | $H_c$ (A/m) | $M_s$ ($10^3$ kA/m) |
|---|---|---|---|
| "Pure" $\alpha$-Fe ($\approx$99%) | $\approx 10^3$ | 80 | 1.71 |
| Pure $\alpha$-Fe ($\approx$99.99%) | $2 \times 10^5$ | 0.8 | 1.71 |
| 78 Permalloy (78Ni, 22Fe) | $\approx 10^5$ | 4 | 0.86 |
| Supermalloy (79Ni, 16Fe, 5Mo) | $\approx 10^6$ | 0.16 | 0.63 |
| Mumetal (77Ni, 18Fe, 5Cu) | $2.4 \times 10^5$ | 2 | $\approx$0.5 |
| Hipernik (50Ni, 50Fe) | $7 \times 10^4$ | 4 | 1.27 |
| Silicon-iron (97Fe, 3Si) (oriented) | $4 \times 10^4$ | 8 | 1.6 |
| Amorphous $Fe_{80}B_{11}Si_9$ | — | 2 | 1.27 |

*Source:* Data for $Fe_{80}B_{11}Si_9$ from N. Cristofaro, *Mater. Res. Soc. Bull.*, May 1998, p. 50; remaining data from A. Chikazumi, *Physics of Magnetism*, Wiley, New York, 1964, p. 494.

[a]The compositions of the alloys are given in weight percent unless otherwise stated.

[b]The maximum relative magnetic permeability $\mu_r$(max) is expressed here in units of $\mu_0 = 4\pi \times 10^{-7}$ N/A$^2$ and corresponds to the maximum value of $B/H$ on the hysteresis loop in the first quadrant taken in increasing field.

Purified Fe can be considered to be one of the very high permeability soft magnetic materials, even though its magnetic anisotropy and magnetostriction are both nonzero. Drawbacks to the widespread use of pure Fe are its relatively low resistivity $\rho \approx 10^{-7}$ $\Omega$·m, a problem when eddy current losses are important, and the expense associated with purification and with other treatments, such as careful annealing to relieve strain. Corrosion of pure Fe is another well-known problem. Fe-based magnetic alloys such as Fe–Ni, Fe–Co, and Fe–Si can have even better properties than those of pure Fe and are also less expensive to produce, being less sensitive than pure Fe to the level of impurities.

The reason that "pure" BCC $\alpha$-Fe is so sensitive to impurities and defects is related primarily to the fact that its intrinsic magnetocrystalline anisotropy coefficient $K_1$ and magnetostriction $\lambda$ are both nonzero, with $K_1 > 0$ and $\lambda_{100} > 0$. By alloying BCC $\alpha$-Fe with FCC Ni, which has $K_1$ and $\lambda_{100}$ both $< 0$, solid-solution FCC Fe–Ni alloys with compositions near 78 wt % Ni can be produced that have intrinsic magnetic anisotropies and magnetostrictions which are much smaller than found in either of the pure metals. The alloy with 78 wt % Ni is known as 78 Permalloy and is used when maximum permeability is desired. When high values of $M_s$ are more important, the content of Fe atoms with larger magnetic moments ($2.2\mu_B$ versus $0.6\mu_B$ for Ni) must be higher, so 45 to 50 wt % Ni alloys are often used. Examples include 45 Permalloy with 45 wt % Ni and Hypernik with 50 wt % Ni (see Table W17.4).

The advantage of very low magnetocrystalline anisotropy for obtaining magnetically soft materials is that for $K \approx 0$ the domain wall thickness $\delta$ is much larger than the typical size of any defect [see Eq. (17.6)]. In this case the interactions of defects such as precipitates or inclusions with domain walls is much weaker, so the effects of pinning are greatly decreased. Low magnetic anisotropy can thus help to minimize the effects of structural imperfections.

The useful FCC Fe–Ni alloys with Ni concentrations greater than 30 wt % have magnetic properties that are usually very sensitive to thermal and mechanical processing treatments and to the presence of impurities. They are ordinarily annealed at high temperatures, above $T = 900$ to 1000°C, and then cooled rapidly to avoid the occurrence of long-range chemical ordering (e.g., formation of the $FeNi_3$ phase). The problem associated with ordering is that the magnetocrystalline anisotropy in the ordered $FeNi_3$ phase is much higher than in the disordered alloys. The disordered FCC phase which is desired can also be retained by the addition of a few at % of transition metal impurities, such as Cu, Cr, or Mo.

Alloys with special properties can be obtained by the addition of elements such as Cu and Mo to Fe–Ni. The alloy Supermalloy, which is obtained by adding Mo to Fe–Ni, corresponds to 79 wt % Ni, 16 wt % Fe, and 5 wt % Mo. Supermalloy has a much higher initial permeability, lower electrical resistivity, and requires simpler heat treatment than do the permalloys. A very useful alloy for magnetic shielding is Mumetal, typically 77 wt % Ni, 18 wt % Fe, and 5 wt % Cu. One of the advantages of adding Cu to Fe–Ni is the increased capability for mechanical working of the resulting alloys.

The 35 at % Ni FCC Fe–Ni alloy known as Invar, with $T_C \approx 250$ to 300°C, has an extremely low thermal expansion coefficient $\alpha$ at room temperature, $\approx 10^{-6}$ $K^{-1}$, an order of magnitude below the values of $\alpha$ for either pure Ni or pure Fe. This "*Invar anomaly*" associated with a low value for $\alpha$ apparently results from cancellation of the usually positive lattice thermal expansion by a negative magnetostrictive

strain contribution resulting from decrease of the spontaneous magnetization $M_s$ in the temperature range just below $T_C$. Above $T_C$ the thermal expansion increases to normal values in the paramagnetic state where the magnetostriction is small.

At the same time that the Invar anomaly or effect occurs, an anomaly in the spontaneous volume magnetostriction $\Delta V/V$ is also observed in these alloys. It is believed that a magnetic moment–volume instability may play an important role in the Invar effect. It has been predicted that in FCC $\gamma$-Fe there can exist two different ferromagnetic states, one a high-spin state with large magnetic moment and large volume and another a low-spin state with low magnetic moment and low volume. In Invar the energy separation between the high spin–high volume state and the low spin–low volume state lying at higher energy is not large, and therefore the low spin-low volume state is thermally accessible. In this way a negative magnetic contribution to the normally positive thermal expansion can appear.

A wide variety of 3*d* transition metal alloys show Invar-type behavior.[†] They have found important applications due to their dimensional stability, including in precision instruments, springs, glass-to-metal seals, and bimetallic applications. Alloys with exceptional elastic stability (e.g., the Fe–Ni alloys known as Elinvar with 40 to 45 at % Ni), find applications in springs, electronic instruments, tuning forks, and so on. Additional elements such as Be, Mn, Mo, Si, and Se are often added to these alloys for hardening purposes and to prevent aging effects.

Fe-Co alloys are also of interest as soft magnetic materials, with useful materials including Permendur (2% V–FeCo) and Hiperco (65Fe, 35Co). In Permendur, vanadium is added to the equiatomic FeCo alloy to increase the resistivity and the ease of fabrication, both of which are low in FeCo, due to the tendency for an order–disorder transition to occur as this alloy is cooled or even quenched. Hiperco has the highest $M_s$ in the alloy series, as can be seen in Fig. 17.17.

***Fe–Si Alloys.*** Although the Fe–Ni alloys just discussed can be prepared with a wide range of magnetic, mechanical, and thermal properties suitable for many applications, Fe-Si alloys are often used in their place — primarily for economic and not physical reasons. The addition of 1 to 4 wt % Si to Fe leads to desired increases in the permeability, the electrical resistivity, and the stability of the magnetic properties as well as a decrease in the coercive field. Drawbacks to the use of Si as an alloying element in Fe include a decrease in the magnetization, essentially a dilution effect associated with the addition of a nonmagnetic element, and an increase in brittleness. The primary benefit related to the addition of Si is the reduction of eddy current losses.

The preferred Fe–Si alloys contain only 1 to 4 wt % Si since alloys having higher Si contents are too brittle to be worked into the desired sheet form. Improved magnetic properties in these low-Si-content alloys can be achieved by the proper mechanical and thermal treatment. Hot rolling and annealing can be used to obtain a desired mechanical texture in polycrystalline sheets. When the resulting texture is (110) [001] [i.e., having the (110) plane parallel to the surface of the sheet with the grains having their [001] directions preferentially aligned parallel to each other], the grain-oriented sheets can be more readily magnetized into a uniform state. This is possible because the [001] direction corresponds to one of the easy axes of magnetization in $\alpha$-Fe. The oriented

[†] For a useful recent review of Invar, see E. F. Wassermann, Chapter 3 in K. H. J. Buschow and E. P. Wohlfarth, eds., *Ferromagnetic Materials*, North-Holland, Amsterdam, 1990.

Fe-Si alloy thus obtained has magnetic properties which are much superior to those of an unoriented alloy.

The 6.4 wt % Si alloy actually has superior magnetic and electrical properties compared to the alloys with lower Si contents. The problem with brittleness at this high Si content can be overcome if additional Si can be incorporated into an existing 3 wt % Si sheet which requires no further mechanical treatments. This can be accomplished by deposition of Si onto the surface of the sheet followed by thermal treatments to diffuse and disperse the surface layer of Si into the bulk.

A metallic glass based on Fe and containing both Si and B (i.e., a-$Fe_{80}B_{11}Si_9$) has lower losses and a lower $H_c$ than grain-oriented Fe-3.2 wt % Si steel. Even though the amorphous metal has a lower $T_C$ than the Fe–Si alloy, 665 K as compared to 1019 K, its thermal stability is sufficient for many applications in electrical equipment. The lower losses in a-$Fe_{80}B_{11}Si_9$ are due to its higher electrical resistivity and lower $H_c$. The lower $H_c$ results from the disordered structure and the resulting lack of defects such as grain boundaries and dislocations that would impede the magnetization and demagnetization processes through the pinning of domain walls.

## W17.12 Details on Materials for Read/Write Heads

Magnetic materials that are currently in use in recording heads include the Fe–Ni alloys known as permalloys, Sendust (an Fe–Al–Si alloy), Mn–Zn ferrites, amorphous alloys, and, most recently, thin films in the form of magnetic multilayers or superlattices. The use of the magnetic multilayers is based on the recently discovered giant magnetoresistance effect discussed in Section W17.4.

The permalloys, discussed earlier for their applications in electromagnetic devices, are Fe–Ni alloys that have low magnetic anisotropy and low magnetostriction, both of which contribute to the high permeabilities observed. The permalloy $Fe_{19}Ni_{81}$ is the most widely used material for inductive heads. In addition, $Fe_{19}Ni_{81}$ shows a magnetoresistive effect of about 4%. Susceptibility to corrosion and high wear rates are limitations of the permalloys.

The Fe–Si–Al alloy known as Sendust, with approximately 85 wt % Fe, 10 wt % Si, and 5 wt % Al, has $K_1$ and $\lambda$ both equal to zero and, as a result, can be prepared with $\mu_{\max} = 1.2 \times 10^5 \mu_0$. This alloy is very brittle and its fabrication into useful forms involves the use of compressed powders.

Mn–Zn ferrites (i.e., $Mn_{1-x}Zn_xFe_2O_4$ with $0.25 < x < 0.5$) are insulating and have the high mechanical hardness necessary for applications as head materials. Since they are ferrimagnetic, they have relatively low values of $M_s$. The addition of Zn to $MnFe_2O_4$ lowers $T_C$, which actually results in higher values of the permeability at room temperature. Adding Zn from $x = 0$ up to 0.5 also leads to an increase in $M_s$. This results from the fact that $ZnFe_2O_4$ is a normal spinel, while $MnFe_2O_4$ is the more usual inverse spinel. Therefore, the added Zn atoms displace $Fe^{3+}$ ions from the tetrahedral to the octahedral sites that were formerly occupied by the now-missing $Mn^{2+}$ ions. As a result, complete cancellation of the spins of the $Fe^{3+}$ ions in octahedral sites by the oppositely directed $Fe^{3+}$ spins in tetrahedral sites no longer occurs and $M_s$ increases. Due to their high permeability and insulating properties, $Mn_{0.5}Zn_{0.5}Fe_2O_4$ ferrites are also used in transformers and inductors.

Magnetic multilayers have recently been incorporated into magnetic read-head structures since they exhibit sensitivities to magnetic fields of 100 to 1000 A/m (i.e., a few

oersteds), which can be five times greater than observed in the conventional materials discussed earlier. These multilayer structures may consist of a sandwich of ferromagnetic metals such as NiFe, Co, or both, separated by a layer of Cu that can be 2 to 3 nm thick. One of the ferromagnetic layers is magnetically hardened so that its magnetic moment is pinned (i.e., unaffected by any magnetic fields to which it may be exposed in operation). This can be accomplished, for example, by exchange-coupling this layer to a thin antiferromagnetic layer such as MnFe, MnNi, or NiO through the mechanism of exchange biasing. Since the exchange coupling of the ferromagnetic layers through the 2-nm Cu spacer layer is relatively weak, the magnetic moment of the second, magnetically soft ferromagnetic sensing layer can rotate or switch directions in response to the magnetic field of the transition region on the magnetic disk. In this way the resistance of the magnetic sandwich changes, the presence of the bit is read, and the stored data are recovered. This type of magnetic structure is based on the giant magnetoresistance effect and is known as a *spin valve*. A dual-spin-valve structure that employs pinned films on each side of the sensing layer increases the response of the read head.

## W17.13 Details on Magnetostrictive Materials

The specific materials with important magnetostrictive applications typically contain at least one magnetic rare earth element and often a magnetic transition metal element as well. Examples include Tb, Dy, and $Tb_{1-x}Dy_x$ alloys, Fe-based intermetallic compounds such as $TbFe_2$, $SmFe_2$, and the pseudobinary compound $Tb_{0.3}Dy_{0.7}Fe_2$, and Fe-based amorphous metallic glasses. Some values of the giant magnetostriction observed in these magnetic materials are presented in Table W17.5. Normal values of the dimensionless magnetostriction $\lambda$ are in the range $10^{-6}$ to $10^{-5}$ for most ferromagnetic and ferrimagnetic materials.

**TABLE W17.5 Magnetic Materials with Giant Magnetostrictions[a]**

| Material | $\frac{3\lambda_s}{2}(10^{-6})$ |
|---|---|
| Dy (78 K) | 1400 |
| Tb (78 K) | 1250 |
| $TbFe_2$ | 2630 |
| $SmFe_2$ | −2340 |
| $DyFe_2$ | 650 |
| $Tb_{0.3}Dy_{0.7}Fe_2$ (Terfenol-D) | ≈2300 |

*Source:* Data from K. B. Hathaway and A. E. Clark, *Mater. Res. Soc. Bull.*, Apr. 1993, p. 36.

[a]These data are for polycrystalline materials at room temperature, unless otherwise noted. The saturation magnetostriction $3\lambda_s/2$ is equal to $\lambda_\parallel - \lambda_\perp$. Here $\lambda_\parallel$ is the magnetostriction measured in the same direction as the applied field $\mathbf{H}$ [i.e., $\delta l(\theta = 0^\circ)/l$] of Eq. (17.29), while $\lambda_\perp$ is the magnetostriction measured in the same direction in the material but with $\mathbf{H}$ rotated by 90° [i.e., $\delta l(\theta = 90^\circ)/l$].

***Rare Earth Metals and Alloys.*** Magnetostrictive strains of up to $10^{-2}$ have been observed in the rare earth metals Tb and Dy below their Curie temperatures $T_C$ of 237 and 179 K, respectively. The magnetostriction of a $Tb_{0.6}Dy_{0.4}$ alloy is shown in Fig. W17.1 as a function of magnetic field. The magnetic and magnetostrictive behaviors of these lanthanide rare earth metals are determined by their partially filled $4f$ shell. The localized, highly anisotropic wavefunctions of the $4f$ electrons, in which the electron spin and orbital motion are strongly coupled to each other via the spin–orbit interaction, lead to strong magnetic anisotropies and also to high magnetostrictions. Note that the orbital part of the magnetic moment is not quenched (i.e., $L \neq 0$) in the rare earths. Of the $4f$ rare earth ions, $Tb^{3+}$ and $Dy^{3+}$ also have the advantage of having two of the largest observed magnetic moments, $9.5\mu_B$ and $10.6\mu_B$, respectively.

***Intermetallic Compounds.*** Since the rare earth (RE) elements and alloys display giant magnetostrictions only below their $T_C$ values (i.e., well below room temperature), considerable effort has gone into finding materials that have correspondingly high magnetostrictions at ambient temperatures. The most successful materials developed so far have been intermetallic compounds and alloys based on rare earths and Fe [e.g., $TbFe_2$ and $(Tb_{0.3}Dy_{0.7})Fe_2$]. These materials also have the advantage of $T_C$ values, which increase as the rare earth concentration is increased.

At room temperature a giant magnetostriction corresponding to $\delta l/l \approx 10^{-3}$ to $10^{-2}$ has been observed in high magnetic fields in the magnetically hard cubic Laves-phase C15 intermetallic compound $TbFe_2$ ($T_C = 704$ K). The largest observed magnetostrictions occur in the $TbFe_2$ and $SmFe_2$ compounds in which the rare earth ions are highly anisotropic and also couple strongly to the Fe ions. The magnetostriction itself is highly anisotropic in these $REFe_2$ materials, with $|\lambda_{111}| \gg |\lambda_{100}|$. It follows that the orientation of the grains is very important for obtaining high magnetostrictions in polycrystalline $REFe_2$ alloys.

The ferromagnetic intermetallic compound $Tb_{0.3}Dy_{0.7}Fe_2$ (Terfenol-D) possesses a room-temperature giant magnetostriction of $\lambda \approx 10^{-3}$ even in low magnetic fields. The particular ratio of Dy to Tb chosen in this compound minimizes the magnetic anisotropy. If present, magnetic anisotropy would require high magnetic fields for magnetic saturation and the full magnetostriction to be achieved. This compensation of the magnetic anisotropy is possible because Tb and Dy have uniaxial magnetocrystalline anisotropy coefficients $K_{u1}$ of opposite sign. The magnetic phase diagram for the pseudobinary $Tb_{1-x}Dy_xFe_2$ system is presented in Fig. W17.15. At high temperatures the alloys are cubic in the paramagnetic phase and become trigonal (rhombohedral) with the easy axes along the $\langle 111 \rangle$ directions in the ferrimagnetic phase below $T_C$. At the composition of Terfenol-D (i.e., $x = 0.7$) a transition to a tetragonal ferrimagnetic phase with spins aligned along the $\langle 100 \rangle$ directions occurs just below room temperature. Choosing a composition where operating at room temperature just above the rhombohedral-to-tetragonal transition is possible allows the alloys to have the desirable attribute of a large magnetostriction in low magnetic fields.

In transductor rods of Terfenol-D the stored magnetoelastic energy density is typically 130 to 200 kJ/m$^3$ and can be as high as 288 kJ/m$^3$ in (111) single crystals. These energy densities correspond to maximum strains of 1.6 to $2.4 \times 10^{-3}$. The fraction of the magnetic energy that can be converted to mechanical or elastic energy, and vice versa, is about 0.6 for Terfenol-D.

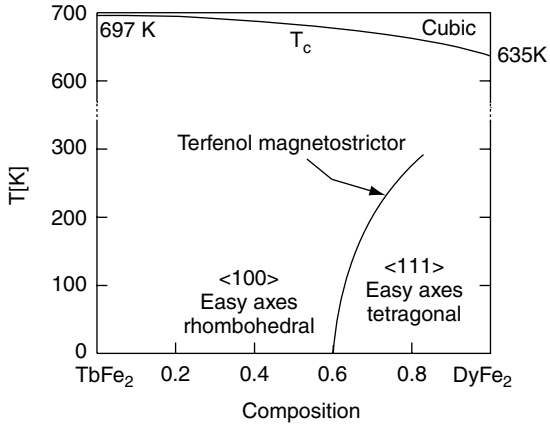


**Figure W17.15.** Magnetic phase diagram of the pseudobinary system $Tb_{1-x}Dy_xFe_2$. [From R. E. Newnham, *Mater. Res. Soc. Bull.*, **22**(5), 20 (1997). Courtesy of A. E. Clark.]

Terfenol-D can also be used in thin-film form for magnetostrictive sensors and transducers in microelectromechanical system (MEMS) technology. Amorphous films of Terfenol-D are magnetically soft and are preferred over crystalline films because the magnetostriction increases rapidly at low magnetic fields with only small hysteresis observed. Due to the high magnetostriction, the magnetic domain microstructure of these films is controlled by the film stress. When compressively stressed, the magnetization **M** in the domains is perpendicular to the film surface, while under tensile stress **M** lies in the plane of the film.

The mechanical damping in the films can be controlled by external magnetic fields since film stress is closely coupled to the direction of the magnetization **M**, and vice versa. Very high values of damping can be achieved by the application of a perpendicular magnetic field to a film under tensile stress as the direction of the magnetization is rotated from parallel to the film's surface to the perpendicular direction.

***Fe-Based Amorphous Metallic Glasses.*** The conversion of magnetic to mechanical energy in amorphous Fe-based metallic glasses (e.g., a Metglas alloy of composition $Fe_{81}B_{13.5}Si_{3.5}C_2$) can be as high as 90% when the amorphous ribbons are annealed in a transverse magnetic field and then cooled rapidly. In this state the ribbons have an induced tranverse magnetic anisotropy. When placed in a longitudinal magnetic field, the domain magnetizations rotate smoothly from the perpendicular to the parallel direction, with no motion of domain walls. The rotation can be accomplished in very low applied fields due to the low anisotropy fields $H_K$ that can be achieved in these amorphous materials. The ribbons elongate due to their positive magnetostriction.

## W17.14 Dilute Magnetic Semiconductors

An interesting class of magnetic materials from a fundamental point of view is the group II–VI semiconductors, such as ZnS, ZnSe, CdS, CdTe, HgS, and HgTe, diluted with Mn atoms which enter these zincblende structures as random substitutional replacements for the divalent Zn or Hg ions. In $Zn_{1-x}Mn_xS$ or $Hg_{1-x}Mn_xTe$, the $Mn^{2+}$ ions with spin $S = \frac{5}{2}$ interact antiferromagnetically with each other via an indirect superexchange

interaction through the bonding electrons associated with the S or Te anions. The $Mn^{2+}$ ions also interact with the conduction-band $s$ and $p$ electrons via the $sp$–$d$ interaction. This is essentially just the $s$–$d$ interaction described in Chapter 9, which plays a critical role in the indirect RKKY interaction between pairs of magnetic ions in metals.

The magnetic behavior of these dilute magnetic semiconductors is paramagnetic for low Mn concentrations (e.g., $x \approx 0.15$ to 0.2 for $Cd_{1-x}Mn_xTe$). At higher Mn concentration the behavior corresponds to that of a disordered antiferromagnet (i.e., a type of spin glass in a semiconducting host). The $sp$–$d$ interaction leads to interesting electrical and optical properties for the $s$ and $p$ conduction-band electrons, including a pronounced magnetoresistance and also a giant Faraday rotation. Potential optoelectronic applications for these materials include their use in display technologies and as infrared detectors, magneto-optical materials, and quantum-well lasers. Other applications of these materials may involve exploiting the spin of the electron in solid-state devices, an area known as *spintronics*. So far it has proven to be difficult to dope these II–VI magnetic semiconductors $n$- and $p$-type.

Recently, it has been possible to deposit films of $Ga_{1-x}Mn_xAs$ with Mn concentrations above the solubility limit via low-temperature molecular beam epitaxy. The Mn atoms in these alloys provide both magnetic moments and hole doping.

## REFERENCES

Aharoni, A., *Introduction to the Theory of Ferromagnetism*, Clarendon Press, Oxford, 1996.

Chikazumi, S., *Physics of Magnetism*, Wiley, New York, 1964.

Craig, A. E., Optical modulation: magneto-optical devices, in K. Chang, ed., *Handbook of Microwave and Optical Components*, Vol. 4, Wiley, New York, 1991.

## PROBLEMS

**W17.1** **(a)** Derive the results for the domain width $d$ and energy $U$ given in Eqs. (W17.3) and (W17.4), respectively.

**(b)** Show also that $U$ given in Eq. (W17.4) for the domain structure shown in Fig. 17.2*b* will be lower than $U_m$ for a single domain given in Eq. (17.4) as long as the thickness $t$ is not too small. Calculate the value of the critical thickness $t_c$.

**(c)** Use the parameters appropriate for Fe at $T = 300$ K to calculate $t_c$. [*Hint:* See the data for Fe at $T = 300$ K given following Eq. (17.6).]

**W17.2** **(a)** For the precession of the magnetization vector **M** in a magnetic field **H** in the $z$ direction, as expressed by equation of motion (W17.17) and shown schematically in Fig. W17.5, show that the three components of **M** have the following equations of motion:

$$\frac{dM_x}{dt} = -\gamma\mu_0 M_y H, \qquad \frac{dM_y}{dt} = +\gamma\mu_0 M_x H, \qquad \frac{dM_z}{dt} = 0.$$

**(b)** Using the trial solutions $M_x(t) = M_\perp \cos\omega t$ and $M_y(t) = M_\perp \sin\omega t$, show that $\omega = \omega_r = \gamma\mu_0 H$.

**(c)** Calculate $\omega_r$ for $g = 2$ and $H = 10^3$ kA/m. To what type of electromagnetic radiation does this correspond?

**W17.3** Consider a permanent magnet in the form of a toroid with an air gap, as shown schematically in Fig. W17.6.

**(a)** If $l_g$ and $A_g$ are the length and cross-sectional area of the air gap, respectively, and $l$ and $A$ are the corresponding values for the magnet, use elementary equations of electromagnetic theory (i.e., $\oint \mathbf{H} \cdot d\mathbf{l} = \mu_0 I$ and $\int \mathbf{B} \cdot d\mathbf{A} = \Phi$) to show that $B/H = -B_g l A_g / H_g l_g A = -\mu_0 l A_g / l_g A$, where $B_g = \mu_0 H_g$ corresponds to the induction in the air gap and $B = \mu H$ corresponds to the induction in the magnet.

**(b)** By comparing this result with Eq. (W17.23), show that $(1 - N)/N = lA_g/Al_g$.

**(c)** Show that the limit $N \ll 1$ corresponds to $l_g \ll l$ [e.g., a very narrow air gap (assuming that $A_g \approx A$)].

**W17.4** For a certain permanent magnet the demagnetization curve in the second quadrant of the $B$–$H$ loop can be described approximately by $B(H) = B_r(1 - |H|^2/H_c'^2)$ with $B_r = 1.25$ T and $H_c' = 500$ kA/m.

**(a)** Calculate the maximum energy product $(BH)_{\max}$ for this material in units of kJ/m$^3$.

**(b)** What demagnetization coefficient $N$ should be chosen for this magnet so that in the absence of an external magnetic field, $(BH) = (BH)_{\max}$ at its operating point?

**(c)** What is the magnetization $M$ in the magnet at this operating point?